Direct strength method for web crippling—Lipped channels under EOF and IOF loading

Direct Strength Method for Web Crippling—Lipped Channels under EOF and IOF loading

Heurkens*, R.A.J., Hofmeyer*, H., Mahendran**, M., Snijder*, H.H.

* Eindhoven University of Technology, Eindhoven, The Netherlands
** Queensland University of Technology, Brisbane, Australia

Abstract
To apply the Direct Strength Method (DSM) to web crippling of lipped channel sections, experiments were recently conducted under EOF and IOF loading conditions. In the research presented here, finite element models were first developed to predict the elastic buckling loads and the elasto-plastic behaviour, both of the experiments and an extended data set. New first- and second-order elasto-plastic theoretical models describing the plastic mechanism initiation of a 2D cross-sectional strip of the lipped channel sections were then developed. Subsequently these 2D cross-sectional models were transformed to full 3D models by using modelled yield line patterns as observed in the finite element simulations. Both the first- and second-order 3D models correlate well with the full section simulations. DSM equations were calibrated based on the results from the simulations, using several alternatives for the yield load as needed in the DSM: a first yield load from the finite element simulations; a rigid-plastic mechanism initiation load as used by other researchers; and a first-order elasto-plastic mechanism initiation load via the above theoretical models. Finally, these calibrated DSM equations were compared with the theoretical models, design codes, and a basic Merchant-Rankine approach. For the DSM, the first order rigid-plastic yield load, most appropriate for the DSM and used by other researchers also, performs best for IOF load cases. For EOF load cases, however, using the first-order elasto-plastic load in the DSM gives best results. Taking these different yield loads for the different cases then, the DSM outperforms Eurocode, AISI S100, and the basic Merchant Rankine predictions. The DSM is intuitively and relatively easy to use, and this paper shows that widening its scope to web crippling of lipped channel sections is possible. Importantly, this paper steps into the discussion for a certain type of yield load to be used in the DSM for web crippling, and gives several arguments to consider the rigid-plastic mechanism initiation load.

Keywords
Lipped Channel Sections; Web crippling; End One Flange (EOF) loading; Interior One Flange (IOF) loading; Experiments; Finite Element Simulations; Direct Strength Method (DSM)

1 Introduction

Thin-walled steel structural members are manufactured from thin steel plates cold-formed via roll-forming machines or press or bending brake operations. Hence they can be produced economically and with easy to optimise cross-sectional geometries. Thin-walled members are susceptible to different types of instabilities, e.g. global, distortional, and local buckling. Under support reactions or concentrated forces, they can fail due to local indentation or even crushing of the cross-section, often referred to as web crippling.

Recent experimental studies by Young and Hancock (2001), Gunalan and Mahendran (2015), Keerthan et al. (2014), Sundararajah et al. (2015), among others, have shown that the current empirical design rules for web crippling based on curve-fitting of experimental results (Prabakaran and Schuster, 1998) and presented in the 'North American Specification for the Design of Cold-Formed Steel Structural Members' AISI S100 (AISI, 2016), are not always conservative. The first reason is considered to be the inconsistent experimental setup used in the studies on which the design equations are based. To avoid these inconsistencies in future experimental studies, the American Iron and Steel Institute has issued AISI S909 (AISI, 2013), a dedicated standard for web crippling experiments. The second reason is that several of the data sets that were considered for the calibration of the expressions contained a small number of specimens.

For thin-walled cold-formed steel structural members in in-plane compression, conventional design rules are based on the semi-empirical effective width method of von Kármán et al. (1932) and Winter (1947). However, this method becomes more complex and prone to inaccuracies for modern cold-formed members that have stiffeners in longitudinal and transverse directions. Therefore, an alternative design method was developed by Schafer and Peköz (1998), the Direct Strength Method (DSM). As also found by Hancock et al. (1994), a clear trend exists between the normalized strength χ (the ratio of the experimental bending strength to the yield moment) and the member slenderness λ

(the square root of the ratio of the yield moment divided by the critical bending moment) as typically shown in figure 1. In this figure, flexural bending test results of members with a variety of cross-sections obtained from several researchers are shown. For the critical bending moment, the finite strip method has been used, taking into account potentially occurring global, distortional, and local buckling modes. The observed trend seems to be valid for members in pure compression also (Anil Kumar & Kalyanaraman, 2010; Becque et al, 2008; Kwon et al, 2009; Moen & Schafer, 2009; Ranawaka & Mahendran, 2009; Shahbazian & Wang, 2011; Yang & Hancock, 2004; Yap & Hancock, 2011). Hence, the concept of the DSM is to utilize this trend to predict the nominal strength of a member based on (a) the yield load and (b) the local, distortional, and global buckling loads, all using gross cross-sectional properties.

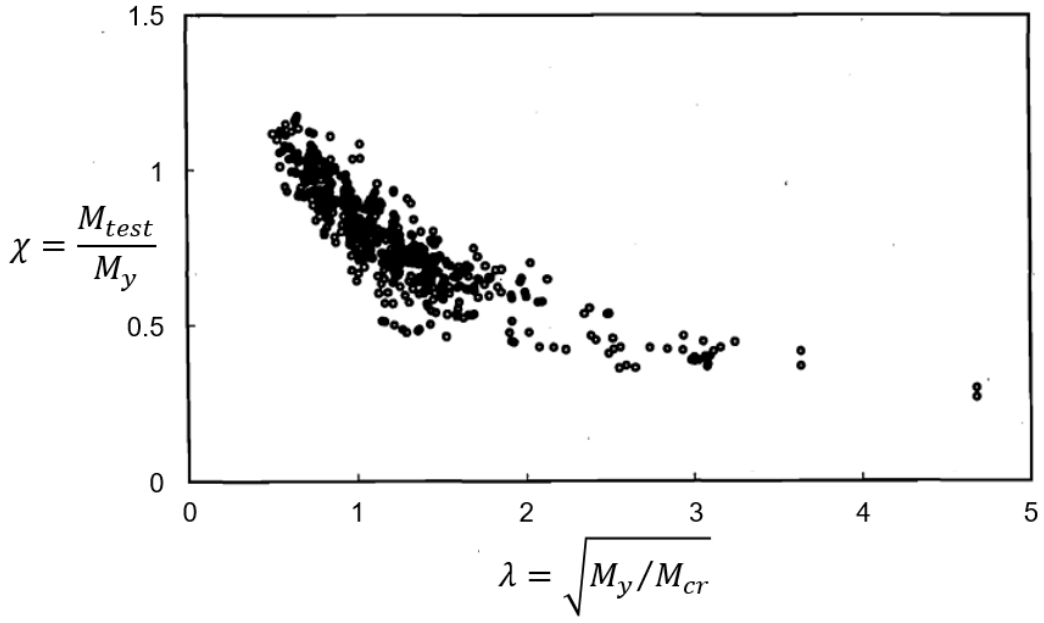

Figure 1. Normalized strength versus Slenderness plot using experimental data (Schafer and Peköz, 1998)

Since 2004, the North American Specification AISI S100 (AISI, 2016) allows the DSM to be used for determining the nominal axial and flexural strengths of columns and beams. To determine a nominal axial compressive strength P_n, a critical buckling load P_{cr} and a yield load P_y are required as shown by equation (1) expressed in the general format. Factors k_i are determined by calibrating against experimental data. For each of the three buckling cases (local, distortional, and global buckling), a similar equation exists, and the equation giving the minimum value governs. Despite some possible limitations as pointed out by Rusch and Lindner (2001) and Schafer (2008) himself, the DSM has shown the potential to provide an easy and accurate method for complex cold-formed steel members.

$$P_n = \left(1 - k_1 \cdot \left(\frac{P_{cr}}{P_y}\right)^{k_2}\right) \cdot \left(\frac{P_{cr}}{P_y}\right)^{k_2} \cdot P_y \qquad (1)$$

Duarte and Silvestre (2013), Keerthan et al. (2014), and Natário et al. (2015) have extended the DSM for specific types of web crippling, which is challenging for the following two reasons. Firstly, the DSM is clearly meant for situations where both instability and (yield) strength play an important role in the final strength. However, although member webs are under in-plane compression in the case of web crippling (thus suggesting instability issues), load application via the corner radii is eccentric to such an extent that actually a strength problem governs, and (local) web instability may be less important. Secondly, a critical buckling load and a yield load are required as input for the DSM. Although no method is prescribed for obtaining the aforementioned loads, the critical buckling load is usually determined by specific finite-strip software. For cases of axial compression, bending, or their combination, often the first yield load is used. For web crippling, however, several possibilities exist to formulate a yield load, e.g. via first yield, a yield line mechanism initiation, or a yield line mechanism

ultimate load. Besides, for the prediction of these three yield loads, first, second, or n^{th}-order elastic formulations can be used. For example, Natário et al. (2015) developed a yield line model, similar to Zhou and Young (2006), for lipped channel sections under End Two Flange (ETF) web crippling loading. This model was used to obtain the yield line mechanism initiation load, without taking into account elasticity, for use as the yield load in the DSM.

The contribution of this paper is to follow up the experiments recently conducted by Sundararajah et al. (2017), by an investigation on the use of the DSM for lipped channel sections under EOF and IOF web crippling loading. Section 2 briefly introduces the experiments (Sundararajah *et al*, 2017). These experiments were simulated by finite element models to obtain accurate and consistent predictions of the member buckling, first yield, and ultimate loads, as presented in section 3. In section 4, new theoretical models are discussed for describing the load-web crippling deformation behaviour based on Hofmeyer (2005). These load-web crippling deformation models provide several alternatives for predicting the DSM yield load. These options are then investigated in section 5 giving calibrations of the DSM with respect to the finite element simulations. Finally, conclusions and recommendations are presented in sections 6 and 7 respectively.

2 Experiments

An experimental study was conducted comprising 36 experiments on lipped channel sections subjected to web crippling under EOF and IOF load cases (Sundararajah, 2017; Sundararajah *et al.*, 2017), see table 1 and figure 2. The study used sections with six different C-section types, each cross-section type tested for three Load Bearing Plate (LBP) widths (l_b = 25, 50, and 100 mm) and for both EOF and IOF Load Cases (LC), as shown in Table 1. For each cross-section type, average measured dimensions are also given in this table, with the member length L approximately $3l_b + 3d$, where l_b is the LBP and d the total section depth, and the span L_{span} equal to $2l_b + 3d$.

Table 1. Average measured geometrical and mechanical properties of lipped channel sections (Sundararajah, 2017)

Experiments	f_y [N/mm^2]	t_w [mm]	r_i [mm]	b_f [mm]	b_l [mm]	d [mm]	d_1 [mm]	E [N/mm^2]	r_i / t_w	d_1 / t_w
C10010 × 3 LBP × 2 LC	581	1.03	3.50	50.4	14.3	100.3	91.2	202,398	3.40	88.6
C10015 × 3 LBP × 2 LC	540	1.52	4.00	50.7	15.8	100.5	89.5	207,859	2.63	58.8
C15012 × 3 LBP × 2 LC	556	1.21	4.00	61.9	18.7	150.7	140.3	200,167	3.31	115.9
C15015 × 3 LBP × 2 LC	531	1.52	4.50	61.7	19.1	150.2	138.1	207,474	2.96	90.9
C20019 × 3 LBP × 2 LC	506	1.91	5.00	76.7	21.0	203.4	189.6	234,804	2.62	99.3
C20024 × 3 LBP × 2 LC	526	2.41	5.00	76.4	21.7	203.5	188.7	205,250	2.07	78.3

LBP = load bearing plate, LC = load case, f_y = yield stress, t_w = web thickness, r_i = internal corner radius, b_f = flange width, b_l = lip depth, d = total section depth, d_1 = flat web depth, E = Young's modulus

The experimental set-up was in accordance with the "Standard Test Method for Determining the Web Crippling Strength of Cold-Formed Steel Beams" AISI S909 as shown in figure 2 for IOF loading. However, the load could not be applied at the shear centre for lipped channel sections. Therefore, to minimize the influence of torsion, two sections were positioned toe-to-toe and both flanges were transversely connected with 20×20×3 mm angle section connectors at 1/4th and 3/4th of the member length. To enforce EOF or IOF failure modes, the specimen web parts that were not to fail were reinforced with 10 mm thick steel plates bolted on each side of the web. The steel plate sizes were equal to the corresponding load bearing width and the flat web depth.

The experimentally found web crippling loads were compared with Australian standard AS/NZS 4600 (Joint Technical Committee BD-082, Cold-formed Steel Structures, 2005) being similar to the AISI S100 and Eurocode 3 Part 1-3 predictions (CEN European Committee for Standardization, 2006). It was found that Eurocode 3 gave conservative predictions for both EOF and IOF load cases, whereas AS/NZS 4600 was unconservative for EOF loading and agreed fairly well with the experiments for IOF loading (Sundararajah et al., 2017).

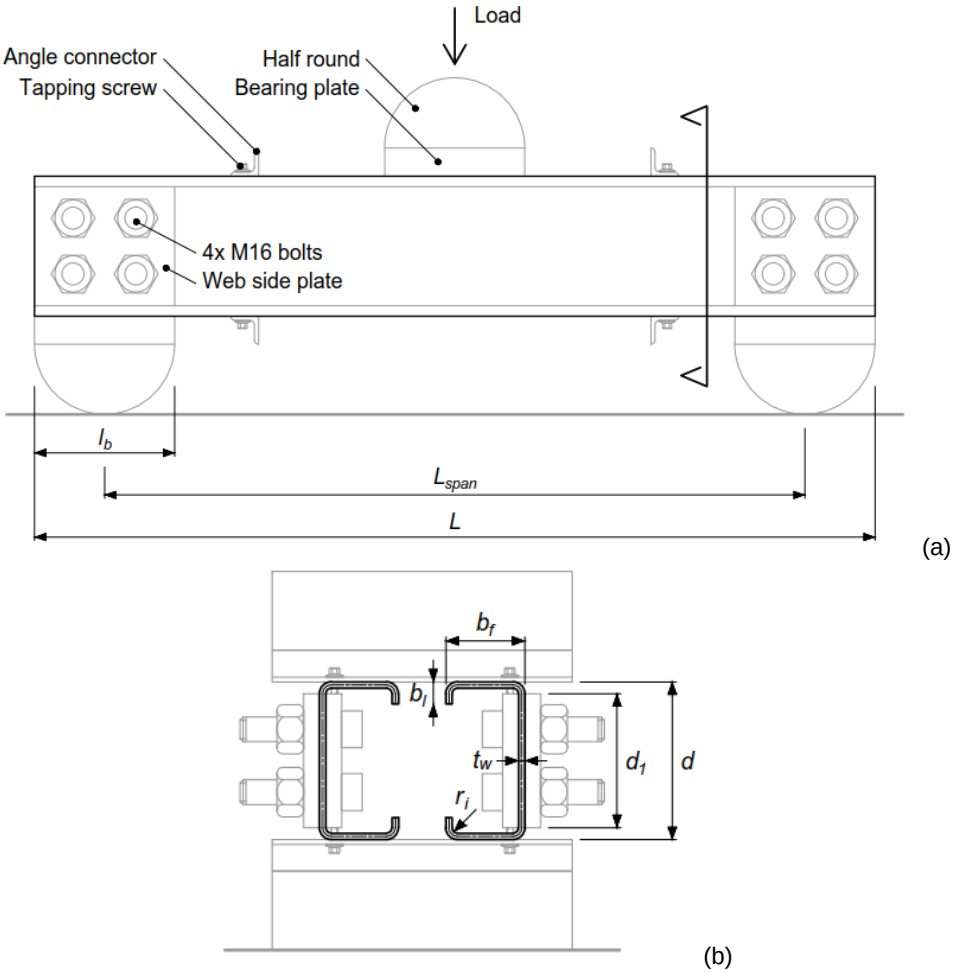

Figure 2. Front view (a) and cross-section (b) of experimental set-up for the IOF load case.

3 Finite element simulations

3.1 Finite element model

Two finite element models were developed: a model for simulating the web crippling behaviour and a model for solely linear buckling analyses. In both models initial geometrical imperfections were not modelled, because the concentrated load as caused by the contact between the load bearing plate and corner radius has a relatively large offset with respect to the web. This itself being a large imperfection, it is believed that other imperfections have little influence on the outcomes of finite element simulations, as shown for a typical case in Heurkens (2017). In order to capture possible longitudinal (figure 3b) and cross-sectional asymmetric (figure 3c) EOF web crippling as observed in some experiments, both toe-to-toe positioned sections, including the load bearing plates, were modelled for the web crippling simulations. As these asymmetries were observed in the plastic stage only, a more efficient quarter model was used for elastic buckling analyses.

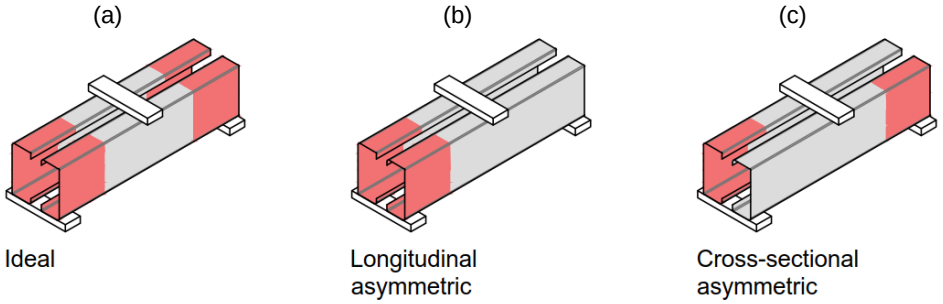

Figure 3. EOF asymmetric failure modes and zones (shown in red): (a) ideal; (b) longitudinal asymmetric; (c) cross-sectional asymmetric.

Sections were modelled with 4-node general-purpose shell elements, using reduced integration, which are suitable for thin shell, large strain analyses: Abaqus S4R (Dassault Systems, 2017). No significant difference was found in the simulation results when full integration was used. The load bearing plates were assumed to be much stiffer compared to the sections, as such modelled by rigid 4-node elements: Abaqus R3D4 (Dassault Systems, 2017). Mesh size was based on a trade-off between computational costs and system (memory) resources on the one hand and solution accuracy on the other: The flat parts in the web crippling model used a fixed mesh size of 2 mm for fine meshed parts and 4 mm for coarse meshed parts (figure 4). Due to less computational costs for the buckling model, only fine meshed parts were used. For the corner radii, the mesh size in the longitudinal direction depended on the adjacent mesh size. Along the radius itself, seven elements were used.

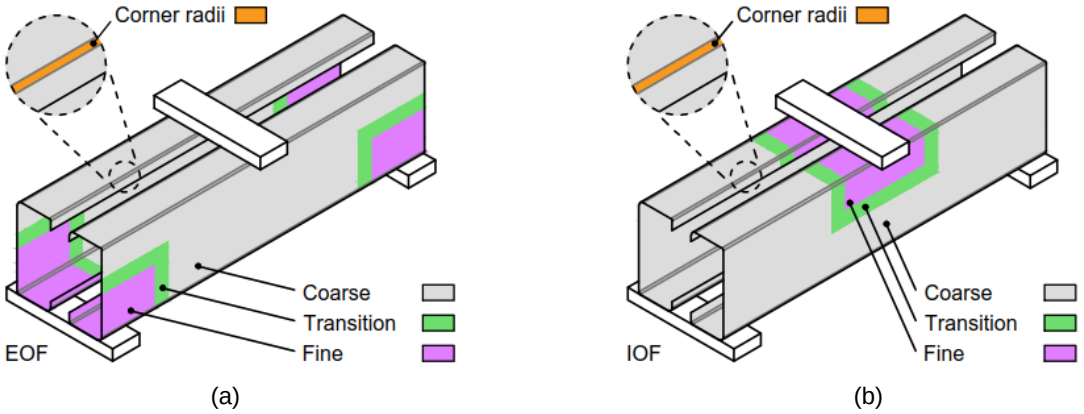

Figure 4. Mesh size distribution for the web crippling model: (a) EOF; (b) IOF

Tensile coupon tests were conducted on the material taken from each cross-section type (Sundararajah, 2017). The engineering stress-strain relations were converted to true values and used for the material property definitions in the finite element program. The declining (necking) part at the end of the stress-strain behaviour was neglected to avoid possible numerical problems.

As mentioned in section 2 on the experimental study, the end or interior web parts were reinforced on both sides with steel plates to enforce either EOF or IOF web crippling failures. This was implemented in the finite element models by assigning at the corresponding positions a web thickness equal to the combined thickness of the steel plates and the web.

Furthermore, the so-called contact and multi-point constraints were defined in the web crippling model. Contact was modelled between the load bearing plates and sections with an assumed friction coefficient of 0.5. The angle section connectors (figure 2) were modelled as the so-called link type Multi-Point Constraint (MPC), which is a pinned link between two nodes.

Figure 5 illustrates the boundary conditions used in the web crippling model. The load bearing plates are rigid bodies for which the boundary conditions are given to their so-called Reference Point (RP). Additionally, to load the section, the top load bearing plate was assigned a prescribed displacement downwards, similar to that used in the experiments.

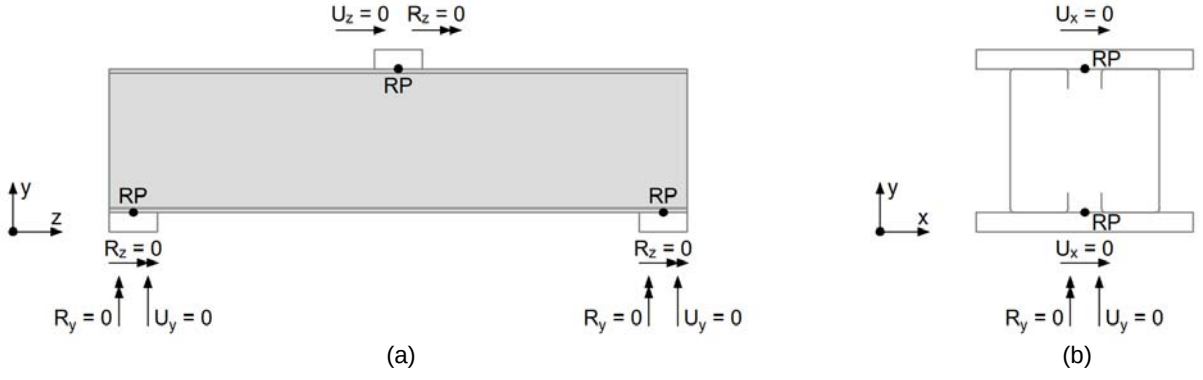

Figure 5. Overview of the assigned boundary conditions in the web crippling model: (a) front view; (b) side view.

In the buckling model however, boundary conditions and unit loads were assigned to lines and points, as shown in figure 6 for the quarter model. Note the single load application at the location where the highest contact forces are found in the web crippling simulations. The corner radii were still modelled with seven elements along the corner.

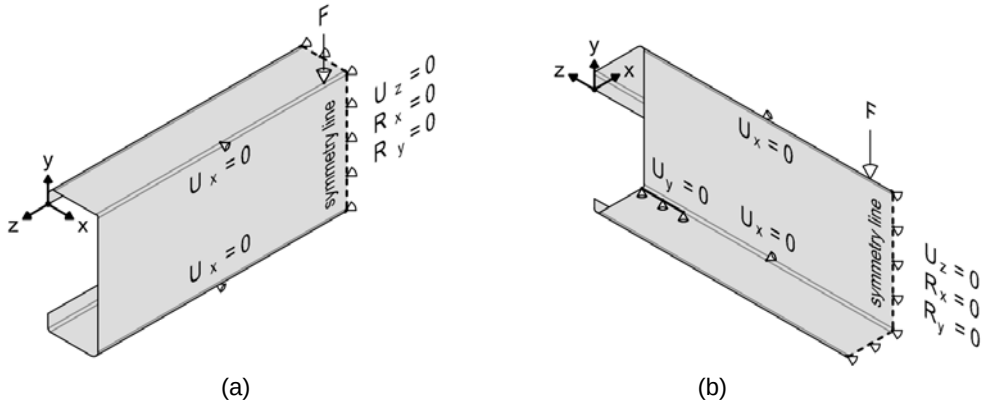

(a) (b)

Figure 6. Overview of the assigned boundary conditions in the buckling model: (a) top plane visible; (b) bottom plane visible.

For the solution, a static implicit procedure was employed for the web crippling model, "Static" as inertia effects and time dependent material effects could be neglected and "Implicit" as only this finds equilibrium states with certainty and an explicit scheme was not found to be necessary (e.g. due to swift contact changes, mode-jumping, or high computational costs). A linear perturbation procedure was employed for the buckling model.

3.2 Validation

Comparing the load versus vertical displacement results from experiments and finite element simulations, a significant difference in elastic stiffness was observed as shown for a typical case in figure 7. This was probably due to the test rig flexibility, inadvertently included in the measured vertical displacements.

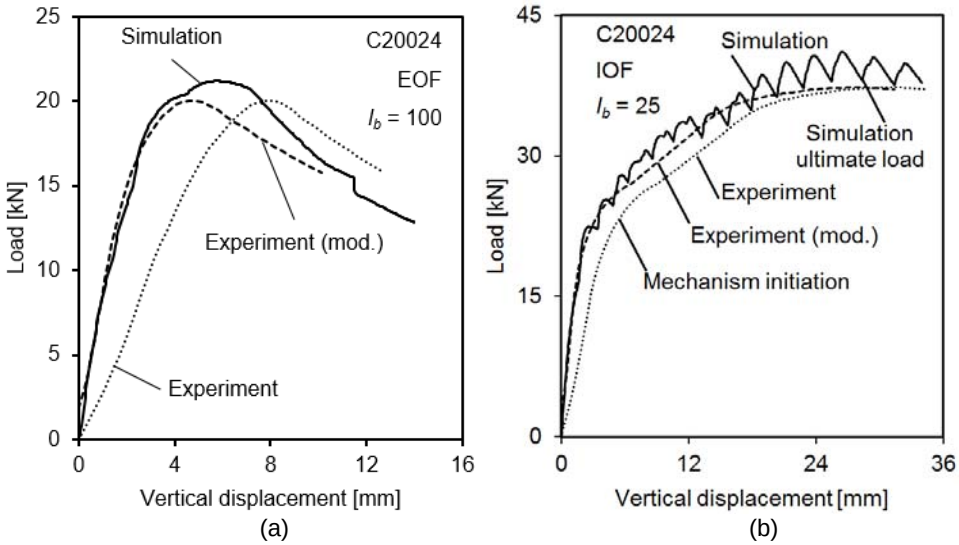

(a) (b)

Figure 7. Load versus vertical displacement curves for C20024 under (a) EOF loading (yield-arc deformation mode, see section 3.4) and (b) IOF loading (rolling deformation mode, see section 3.4).

To account for this test rig flexibility, the experimental set-up was schematized by two springs in series, one modelling the test rig and one modelling the section, with spring stiffness k_{tr} and k_{se}, respectively, yielding a combined stiffness as shown in equation (2).

$$\frac{1}{k_{tr+se}} = \frac{1}{k_{tr}} + \frac{1}{k_{se}} \qquad (2)$$

From the experiments, the combined stiffness is known. By assuming a single fixed test rig flexibility for the EOF web crippling experiments and another fixed one for the IOF web crippling experiments, the two test rig flexibilities were predicted by minimizing the sum of all squared residuals between all the finite element elastic curves and the adjusted experimental curves. For most experiments, this resulted in a good agreement between the finite element simulation and the experiment as shown in figure 7.

For EOF loading the finite element load-vertical displacement curves were relatively smooth, and the ultimate load could be taken as the maximum load found. In some of the IOF load cases though, the load-vertical displacement curves were non-monotonic due to the inevitably finite number of elements along the corner. As these elements also have only a limited number of integration points were plasticity can be described, the movement of the yield lines (as shown in figure 10(d) and 10(e)) is simulated in a somewhat stepwise fashion. As the local minima of the finite element curves were closest to the experimental curves, the maximum local minimum has been taken (visually) as the ultimate load, see figure 7(b). This approach was further verified by the fact that for both EOF and IOF load cases a very good agreement was found between the experiments and the simulations as shown in table 2, and by the high correlation coefficient ρ as shown in figure 8.

Table 2. Overview simulation results and comparison with experiments.

Cross-section	l_b	EOF $F_{cr,sim}$	EOF $F_{y,sim}$	EOF $F_{u,sim}$	EOF $F_{u,exp}$	EOF $F_{,y;sim/}$ $F_{u,sim}$	IOF $F_{cr,sim}$	IOF $F_{y,sim}$	IOF $F_{u,sim}$	IOF $F_{u,exp}$	IOF $F_{,y;sim/}$ $F_{u,sim}$
	[mm]	[kN]	[kN]	[kN]	[kN]	[1]	[kN]	[kN]	[kN]	[kN]	[1]
C10010	25	4.46	0.87	3.41	3.92	0.87	9.22	1.29	7.82	8.11	0.96
C10015	25	14.98	1.79	10.17	9.51	1.07	30.23	2.72	14.79	15.52	0.95
C15012	25	4.21	0.99	5.83	5.10	1.14	9.43	1.60	10.34	11.57	0.89
C15015	25	8.49	1.52	6.73	6.96	0.97	18.98	2.23	15.96	15.41	1.04
C20019	25	12.73	2.42	11.28	10.50	1.07	29.98	3.87	26.64	23.99	1.11
C20024	25	21.19	3.43	21.35	17.77	1.20	50.14	5.66	37.12	37.32	0.99
C10010	50	6.03	1.79	3.97	4.22	0.94	10.57	1.70	8.33	8.91	0.93
C10015	50	19.49	2.93	8.62	9.62	0.90	33.37	3.61	14.17	15.05	0.94
C15012	50	5.31	1.88	4.65	5.16	0.90	10.27	1.97	11.97	12.78	0.94
C15015	50	10.86	2.76	7.82	8.75	0.89	20.79	3.21	14.54	13.32	1.09
C20019	50	14.99	4.14	11.70	11.18	1.05	31.02	4.98	21.79	18.19	1.20
C20024	50	25.55	5.73	18.10	18.84	0.96	52.42	6.82	33.99	28.94	1.17
C10010	100	8.20	2.85	4.91	5.14	0.96	13.42	2.31	9.35	9.29	1.01
C10015	100	25.33	4.47	10.51	10.68	0.98	41.47	4.53	17.99	19.81	0.91
C15012	100	7.24	3.47	5.50	6.01	0.92	12.18	2.94	11.77	11.72	1.00
C15015	100	14.77	5.18	9.03	9.61	0.94	24.68	4.51	17.13	16.84	1.02
C20019	100	19.84	7.85	13.25	12.39	1.07	34.49	7.14	24.72	24.72	1.00
C20024	100	34.57	9.46	21.20	20.05	1.06	58.95	9.52	38.86	37.65	1.03

l_b = bearing plate width, $F_{cr,sim}$ = simulation buckling load, $F_{y,sim}$ = simulation first yield load, $F_{u,sim}$ = simulation ultimate load, $F_{u,exp}$ = experimental ultimate load

Failure modes observed in the experiments were simulated correctly as typically shown in figure 9. Also longitudinal asymmetric modes as found in the experiments were correctly reproduced asymmetrically without any predefined imperfections. However, observed experimental cross-sectional asymmetric modes were predicted as ideal (symmetric) in the finite element simulations. This was believed not to be problematic as it was assumed that symmetrical and asymmetrical outcomes do not differ for the results required from the finite element simulations. For example, the ultimate load would not differ as both the external and internal work become half for an asymmetric mode, respectively due to the inclined deflection pattern and due to plasticity occurring at only half the number of locations. This assumption was verified for a single experiment by FE simulations with and without imperfections, these imperfections enforcing the solution towards cross-sectional asymmetry.

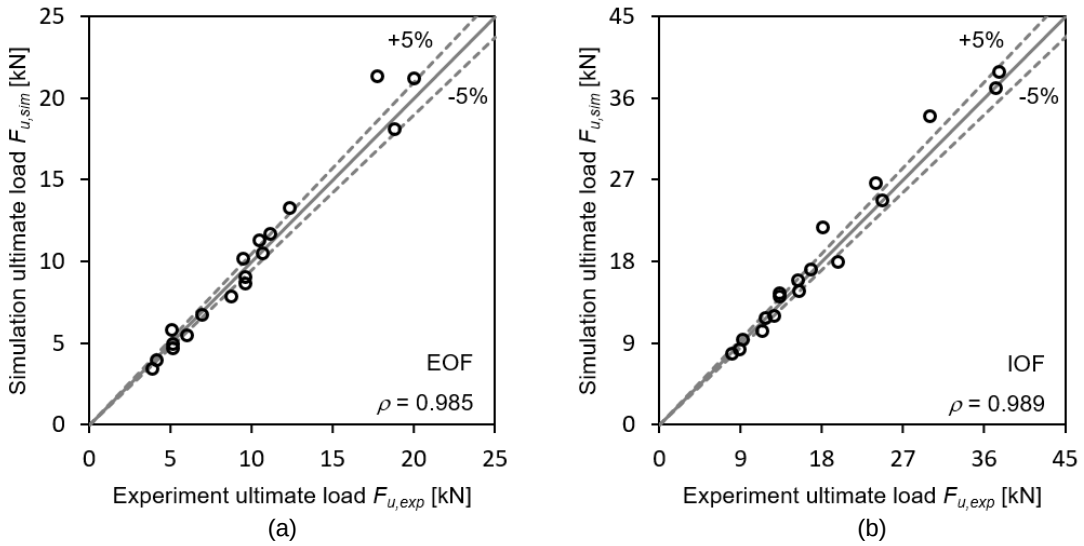

Figure 8. Correlation between experimental and finite element simulation ultimate loads for (a) EOF load cases and (b) IOF load cases.

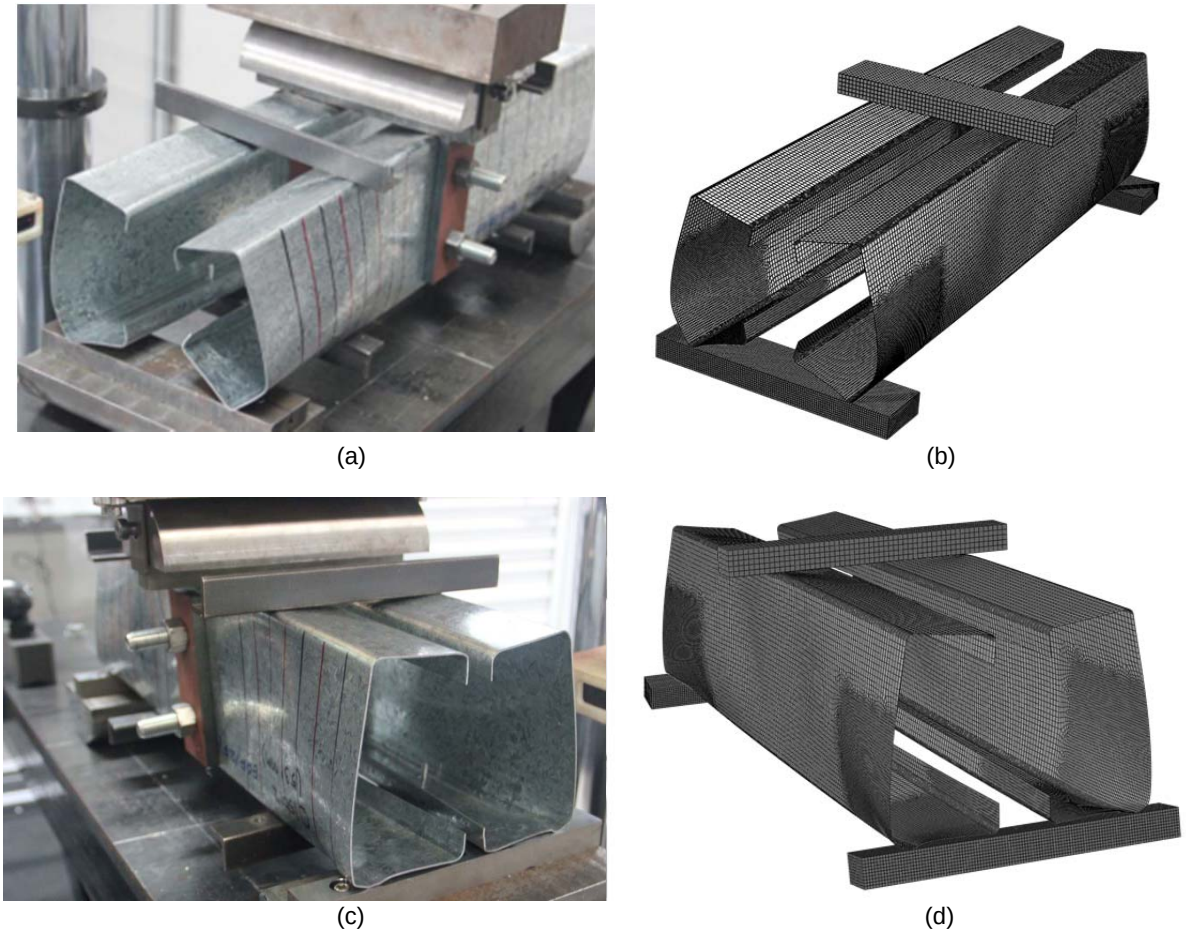

Figure 9. C51012 EOF, (a) experiment and (b) simulation load bearing plate 50 mm (yield-arc deformation mode, see section 3.4), (c) experiment and (d) simulation load bearing plate 25 mm (rolling deformation mode, see section 3.4).

3.3 Extended data set

In the experiments, six different cross-sections were studied, spanning a relative small bandwidth of flat web depth over web thickness ratios d_1 / t_w equal to 58.8 to 115.9. To be able to calibrate the DSM in section 5 with a sufficiently large dataset, the validated finite element model was used to simulate

16 virtual experiments, comprising eight designed cross-sections for EOF and IOF load cases (Table 3).

Table 3. Designed cross-sections for the extended data set.

Simulations (extended)	f_y [N/mm^2]	t_w [mm]	r_i [mm]	b_f [mm]	b_l [mm]	d [mm]	d_1 [mm]	r_i / t_w	d_1 / t_w
C09015 x 1 LBP x 2 LC	540	1.50	3.50	47.3	14.6	90.0	80.0	2.33	53.3
C08015 x 1 LBP x 2 LC	540	1.50	3.50	44.7	14.0	80.0	70.0	2.33	46.7
C07015 x 1 LBP x 2 LC	540	1.50	3.50	42.0	13.4	70.0	60.0	2.33	40.0
C06015 x 1 LBP x 2 LC	540	1.50	3.00	39.4	12.7	59.0	50.0	2.00	33.3
C17012 x 1 LBP x 2 LC	556	1.20	4.50	68.3	19.7	171.4	160.0	3.75	133.3
C19012 x 1 LBP x 2 LC	556	1.20	5.00	73.6	21.0	192.4	180.0	4.17	150.0
C21012 x 1 LBP x 2 LC	556	1.20	5.00	78.9	22.2	212.4	200.0	4.17	166.7
C23012 x 1 LBP x 2 LC	556	1.20	5.50	84.1	23.5	233.4	220.0	4.58	183.3

LBP = load bearing plate, LC = load case, f_y = yield stress, t_w = web thickness, r_i = internal corner radius, b_f = flange width, b_l = lip depth, d = total section depth, d_1 = flat web depth

The designed cross-sections are based on specimens C10015 and C15012 with the lowest and highest d_1 / t_w ratios, respectively. For the designed cross-sections, first the flat web depth was adjusted to alter the d_1 / t_w ratio. Hereafter the internal corner radius r_i, flange width b_f and lip depth b_l were adjusted based on the correlation between these variables and the flat web depth (Heurkens, 2017). Web thickness and yield stress were left unchanged and the load bearing width was chosen as 50 mm.

For both the experiments and the extended data set, the finite element model was used to find the elastic buckling load, the first yield load and the ultimate load, as further explained in section 5 and in detail in Heurkens (2017).

3.4 Yield line pattern specification

In general, for thin-walled steel members in web crippling, two deformation modes can be distinguished: yield-arc and rolling (Bakker and Stark, 1994) as shown in figure 9(a,b) and figure 10 (b,c), and figure 9(c,d), and figure 10(d,e) respectively. The name 'yield-arc' originates from the yield line geometry in the longitudinal direction of the member, which is often shaped like an arc. And in this mode, yield lines more or less keep their initial positions. In contrast, the rolling deformation mode is characterized by moving yield lines near the radius-web and radius-flange junctions.

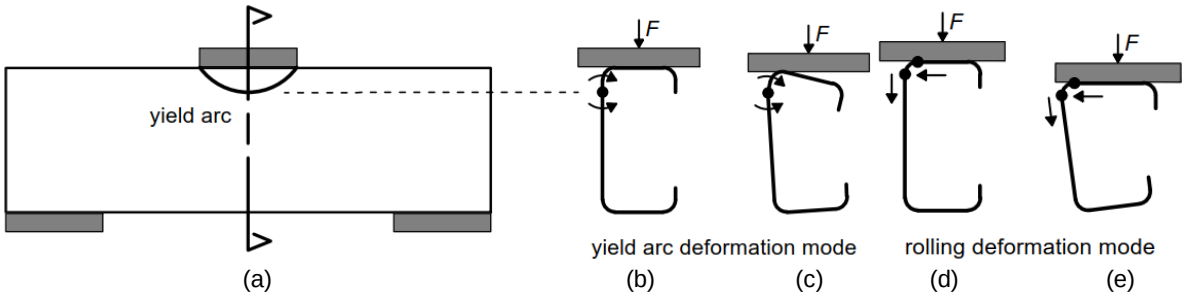

Figure 10. Yield-arc and rolling deformation modes: (a) front view; (b) yield arc initiation; (c) yield arc deformed; (d) rolling initiation; (e) rolling deformed.

In the load-vertical displacement curves, the two deformation modes are distinct: rolling modes show (at least for short spans) an increasing plastic curve, whereas yield-arc modes tend to (sometimes only slightly) decrease their plastic strength, see figure 7 and Bakker and Stark (1994). Here, for the simulations under the IOF load case, each different load bearing plate width results in a different deformation mode or a combination of modes as shown in table 4, i.e. in the case of a 25 mm load bearing plate, only rolling occurs; a 50 mm load bearing plate results in a yield-arc mode, which transfers to a rolling mode eventually; a 100 mm load bearing plate gives a pure yield-arc mode. For the simulations under the EOF load case, the yield-arc mode occurs regardless of the load bearing plate width. Only for the 25 mm load bearing plate, and only after yield-arc initiation, a transition can be seen towards the rolling mode.

For the development of regression formulae to predict yield line positions for use in the theoretical models of section 4, yield line pattern geometries in the finite element simulations have been

measured. In the EOF simulations, the ultimate load was clearly distinguishable in general, and measurements were conducted at about 80% of the ultimate load left in the post-failure stage for 50 and 100 mm load bearing plates. For 25 mm load bearing plates, measurements were successfully taken just before transition to the rolling deformation mode. In contrast with the EOF simulations, the ultimate load was not always obvious in the IOF load cases, especially when the rolling deformation mode occurred. Nevertheless, in the plastic stage a clear yield line pattern could be recorded for 50 and 100 mm load bearing plates. For 25 mm load bearing plates, where a rolling mode occurred, no information on the yield line position and propagation along the length could be obtained, see table 4.

Table 4. Deformation modes and obtained yield line positions and propagations along the length.

Case l_b [mm]	IOF 25	IOF 50	IOF 100	EOF 25	EOF 50	EOF 100
Mode	Rolling	Yield arc (followed by rolling)	Yield arc	Yield arc (followed rolling)	Yield arc	Yield arc
L_y - r_m	Not found	Found (during plastic stage)	Found (during plastic stage)	Found (just before rolling)	Found (at 80 % after ultimate load)	Found (at 80 % after ultimate load)
L_A	Not found	Found (during plastic stage)	Found (during plastic stage)	Found (just before rolling)	Found (at 80 % after ultimate load)*.	Found (at 80 % after ultimate load)*.

IOF = Interior One Flange, EOF = Exterior One Flange, l_b = load bearing plate width [mm], L_y-r_m = yield line distance in figure 11, L_A = yield line distance in figure 12 and 13, * not found for C10015.

The most important measurement involves the yield line position with respect to the cross-sectional geometry as shown in figure 11. For this position, variable (L_y - r_m) was used instead of L_y, because L_y implicitly includes distance r_m as well, whereas (L_y - r_m) is independent of other variables.

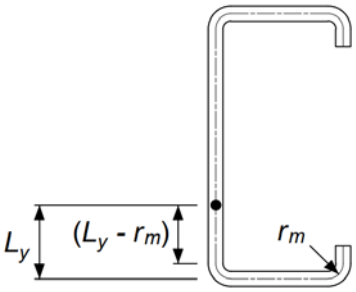

Figure 11. Yield line position.

For the simulations under both EOF and IOF load cases, the (available) measured yield line positions, at the load bearing plate along the length, show a good correlation with the load bearing plate width, with a correlation coefficient ρ = 0.88 and 0.97, respectively. Based on this, a relation between the yield line position and the load bearing width was derived via linear regression (equations (3) and (4)).

$$\left(L_y - r_m\right)_{EOF} = 0.36 \cdot l_b + 1.07 \tag{3}$$

$$\left(L_y - r_m\right)_{IOF} = 0.18 \cdot l_b - 1.36 \tag{4}$$

The second measurement concerns the yield line propagation along the longitudinal direction of the section. For the EOF yield-arc simulations, the yield line pattern is shown schematically in figure 12(a): The yield line starts at the section end and runs horizontally towards the centre. Just before the reinforced web is reached, it inclines downward at about 30°. This yield line pattern is very similar for all 50 and 100 mm load bearing width simulations, whereas for a 25 mm load bearing width, the yield line remained horizontal or inclined upwards, the cause unknown. For the theoretical models in section 4, the yield line geometry will be simplified as shown in figure 12(b), taking into account half the length of the inclined yield line (as such for the model downward or upward inclination of the yield line

becomes irrelevant). The yield line length L_A as such derived from the simulations correlates reasonably with the load bearing plate l_b and span length L_{span} (with a correlation coefficient of ρ = 0.76 and 0.62, respectively), resulting in equation (5) when linear regression is used.

$$L_A = 1.66 \cdot l_b + 0.22 \cdot L_{span} - 35.05 \quad (5)$$

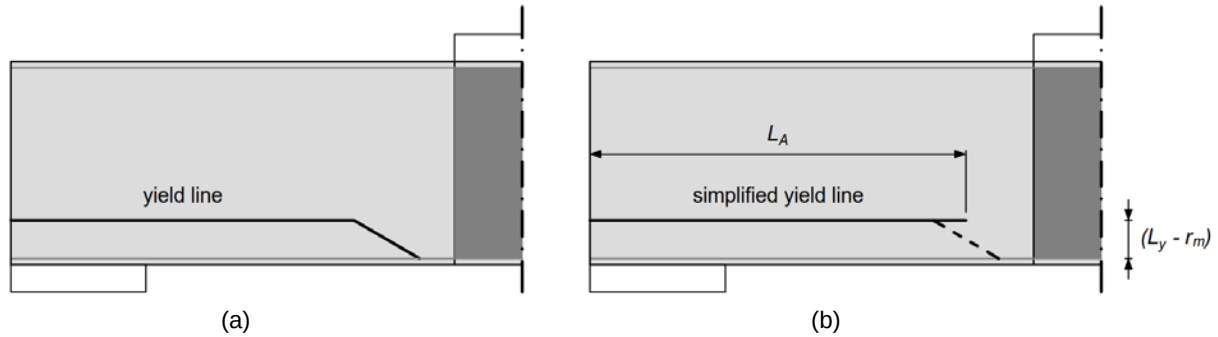

Figure 12. (a) actual yield line pattern for the EOF load case on the left; (b) simplified pattern on the right.

For the IOF yield-arc simulations, the yield line pattern is shown in figure 13(a). Two arc-shaped yield lines occur, one beneath the top load bearing plate and one in the web between the top load bearing plate and the reinforced web at the section end. This pattern occurs for the 50 and 100 mm load bearing plate widths only, as only these simulations deform in accordance with the yield-arc mode. For the C10015 specimens, only the yield line beneath the top load bearing plate was visible. For the theoretical models, beneath the load bearing plate a horizontal yield line will be assumed that inclines upwards to the point where the large arc yield line ends, as shown in figure 13(b). From the available simulation measurements, L_A correlates strongest with the flat web depth d_1 and span length L_{span} (with a correlation coefficient of ρ = 0.80 and 0.82, respectively). Then linear regression results in equation (6). All measurements as found in the finite element simulations and correlations graphs can be found in Heurkens (2017)

$$L_A = 0.38 \cdot d_1 + 0.17 \cdot L_{span} + 47.33 \quad (6)$$

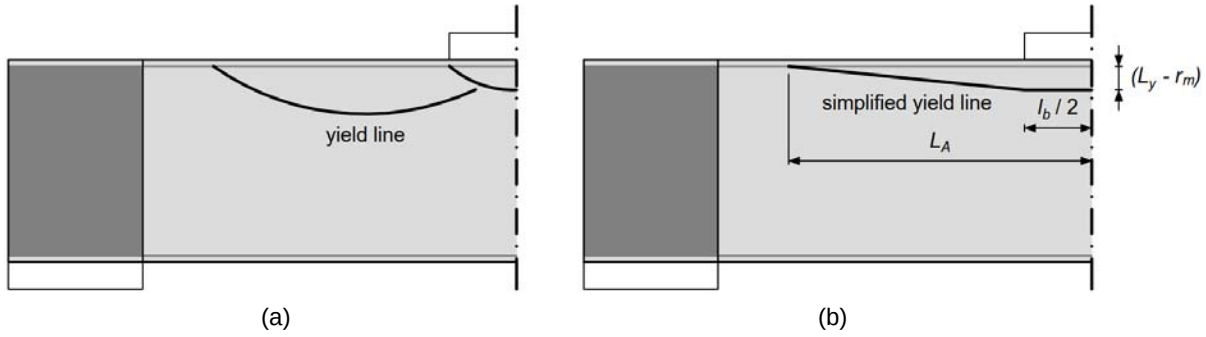

Figure 13. (a) actual yield line pattern for the IOF load case; (b) simplified pattern.

Note that the IOF formulae 4 and 6 are based on the available measurements as indicated in table 4, and thus may not necessarily be applicable in the case of a rolling mode (with l_{lb} = 25 mm).

4 Theoretical models

Theoretical analysis of web crippling is rather complex due to the non-uniform stress distribution in the web-flange junction, possible elastic and inelastic nonlinear buckling of the web and the non-linear material properties of the steel. Nevertheless, attempts have been made for predicting the web crippling plastic mechanism initiation load (Bakker and Stark, 1994); for predicting the ultimate load (Young and Hancock, 1998; Hofmeyer et al., 2002); or to describe the plastic load-web crippling behaviour theoretically (Hofmeyer, 2005). Based on the latter work, the outline of several theoretical models will be presented here for describing the elastic and plastic load-web crippling deformation behaviour of lipped channel sections. Full derivations can be found in Heurkens (2017).

4.1 First order elastic with contact change

Given the short span length of the sections in the experiments, bending deflections along the length are neglected here, making the EOF and IOF loading conditions essentially a two-flange loading condition, figure 14(a). The theoretical models will first be developed 2D, based on the behaviour of a thin strip of the section, with length *dz*. The thin strip is mechanically modelled as an eccentrically loaded column as shown if figure 14(b). This 2D behaviour will then be distributed along the length of the section, providing a 3D description. Note that the theoretical models are a simplification as the web will buckle and behave like a plate, which is not completely taken into account here.

Using first-order elastic beam theory for the mechanical model in figure 14(b), the web displacement and rotation are given by Equations (7) and (8), respectively. Note that for this first-order approach an additional bending moment, as caused by the axial load about the deformations of the web, is not taken into account. With the rotation known, column shortening due to bending, i.e. elastic web crippling deformation, $\Delta d_{m,}$ can be found by Equation (9), and yielding by the expression in Equation (10). Note that this elastic web crippling deformation is valid for small rotations only, because of the Taylor series based approximation of the term involving the radical sign in Equation (9).

$$v(x) = -\frac{F \cdot r_m \cdot x^2}{2 \cdot EI} + \frac{F \cdot r_m \cdot d_{m1} \cdot x}{2 \cdot EI} \tag{7}$$

$$v'(x) = -\frac{F \cdot r_m \cdot x}{EI} + \frac{F \cdot r_m \cdot d_{m1}}{2 \cdot EI} \tag{8}$$

$$\Delta d_m = \int_0^{d_{m1}} \left(\sqrt{1 + \left(v'(x)\right)^2} - 1 \right) \cdot dx \approx \int_0^{d_{m1}} \left(\frac{1}{2} \cdot \left(v'(x)\right)^2 \right) \cdot dx \tag{9}$$

$$\Delta d_m = \frac{{d_{m1}}^3 \cdot {r_m}^2 \cdot F^2}{24 \cdot \left(EI\right)^2} \tag{10}$$

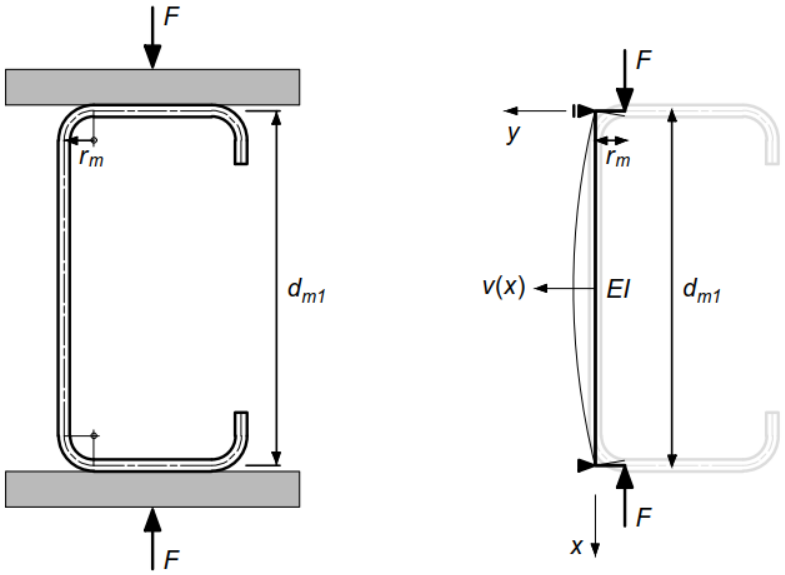

Figure 14. (a) strip of lipped channel section; (b) corresponding mechanical model.

Elastic web crippling deformation will include rotation of the corner radius. Having a rigid and flat loading bearing plate, this rotation causes the applied load to change position from its initial position (at the web-radius junction) towards a position further along the radius. It has been found that this contact change has a significant influence and will therefore be taken into account (Heurkens, 2017). Therefore a linear relationship is assumed in which the eccentricity will be equal to r_m in the case of zero flange rotation and will be zero in the case of $\pi/2$ rad flange rotation, as described by equation

(11) with r_{mi} being the initial eccentricity. Although advanced non-linear solution procedures could be used, a basic incremental scheme was used here: for a step with a small increase of the load, the web crippling deformation and flange rotation were calculated by equation (10) and (8), followed by an update of the eccentricity by equation (11) for the next step, which resulted in a load-web crippling deformation curve. The above model was named M1EC (Model 1st order Elastic with Contact change).

$$r_m = r_{mi} - \frac{2 \cdot r_{mi} \cdot v'(x)\big|_{x=0}}{\pi} \tag{11}$$

4.2 Second order elastic with contact change

For the model as presented in figure 14, Timoshenko and Gere (1985) used second order elastic theory to determine the displacement of the web in *y*-direction, as given by equation (12). Note that this approach takes into account the additional bending moment as caused by the axial load about the deformations of the web. Deriving the displacement function to *x* yields the rotation function (equation (13)).

$$v(x) = r_m \cdot \left(\frac{\sin(k \cdot x)}{\sin(k \cdot d_{m1})} - \frac{x}{d_{m1}} \right) + r_m \cdot \left(\frac{\sin(k \cdot (d_{m1} - x))}{\sin(k \cdot d_{m1})} - \frac{d_{m1} - x}{d_{m1}} \right) \tag{12}$$

$$v'(x) = \frac{k \cdot r_m \cdot \left(-\cos(k \cdot (d_{m1} - x)) + \cos(k \cdot x) \right)}{\sin(d_{m1} \cdot k)} \tag{13}$$

with:

$$k = \sqrt{\frac{F}{EI}} \tag{14}$$

Similar to M1EC, the web crippling deformation Δd_m can be determined by evaluating the integral given by equation (15), resulting in equation (16).

$$\Delta d_m = \int_0^{d_{m1}} \left(\sqrt{1 + (v'(x))^2} - 1 \right) \cdot dx \approx \int_0^{d_{m1}} \left(\frac{1}{2} \cdot (v'(x))^2 \right) \cdot dx \tag{15}$$

$$\Delta d_m = -\frac{k \cdot r_m^{\,2} \cdot \left(-d_{m1} \cdot k + \sin(d_{m1} \cdot k) \right)}{4 \cdot \cos\left(\frac{d_{m1} \cdot k}{2} \right)^2} \tag{16}$$

The inclusion of contact change (and the resulting incremental calculation procedure) of this model is similar to the model M1EC, and thus is given by equation (11). This model is named M2EC (Model 2nd order Elastic with Contact change).

4.3 Yield-arc second order plastic

For a second order plastic model, elastic bending is neglected and plastic bending is thought to be concentrated at one location, figure 15. It is assumed that the corner radii centre points remain on the same vertical line, independent of deformations and yield line location. Although these assumptions do not represent actual behaviour, they have been verified to have little influence on the plastic load-web crippling behaviour (Heurkens, 2017).

As the theoretical models are here used to predict mechanism initiation rather than the full plastic behaviour, and for mechanism initiation the rolling mode can be regarded as a yield-arc mode with a yield line close to the load bearing plate, here it is assumed that the yield-arc second order plastic model is also applicable to the rolling mode.

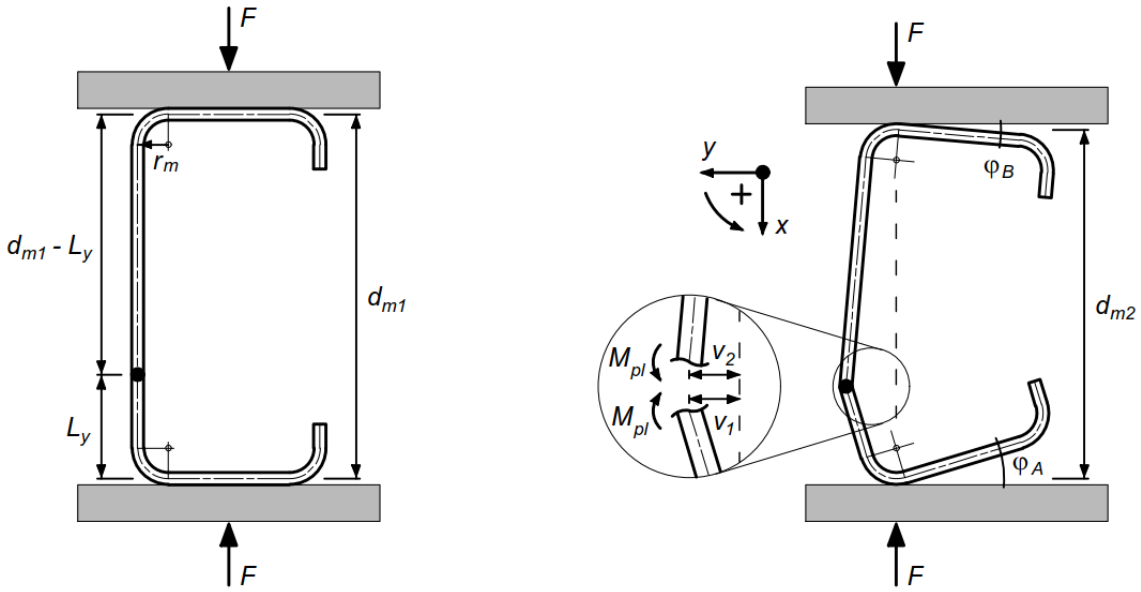

Figure 15. Yield line model of a strip of lipped channel section: (a) initial; (b) deformed.

For a bottom flange rotation φ_A, the out-of-plane web displacement v_1 can be calculated using equation (17). As out-of-plane displacement v_2, given by equation (18), should equal v_1, the top flange rotation φ_B can be determined using equations (17) and (18) iteratively.

$$v_1 = \cos(\varphi_A)\cdot r_m + \sin(\varphi_A)\cdot(L_y - r_m) \tag{17}$$

$$v_2 = \cos(-\varphi_B)\cdot r_m + \sin(-\varphi_B)\cdot(d_{m1} - L_y - r_m) \tag{18}$$

When both flange rotations are known, the reduced height can be calculated by equation (19). Correcting for the original height, the web crippling deformation Δd_m is then given by equation (20).

$$d_{m2} = r_m - \sin(\varphi_A)\cdot r_m + \cos(\varphi_A)\cdot(L_y - r_m) + \cos(-\varphi_B)\cdot(d_{m1} - L_y - r_m) + r_m - \sin(-\varphi_B)\cdot r_m \tag{19}$$

$$\begin{aligned}\Delta d_m &= d_{m1} - d_{m2} = \\ &= d_{m1} - \left(r_m - \sin(\varphi_A)\cdot r_m + \cos(\varphi_A)\cdot(L_y - r_m) + \cos(-\varphi_B)\cdot(d_{m1} - L_y - r_m) + r_m - \sin(-\varphi_B)\cdot r_m\right)\end{aligned} \tag{20}$$

Moment equilibrium of the lower part about the yield line is given by equation (21). With the plastic moment in the yield line by equation (22), the corresponding load for an arbitrary bottom flange rotation can be obtained (equation (23)). This allows for calculating the plastic force-web crippling deformation diagram as follows: for values φ_a equation (17) is used to calculate v_1. As v_1=v_2, rotation φ_b is determined by equation (18). The corresponding load and web crippling deformation can then be predicted by equations (20) and (23). This model is named MA2P (Model yield-Arc 2nd order Plastic).

$$-M_{pl} + F\cdot v_1 = 0 \tag{21}$$

$$M_{pl} = \frac{t_w^{\,2}\cdot f_y}{2\cdot\sqrt{3}} \tag{22}$$

$$F = \frac{t_w^{\,2}\cdot f_y}{2\cdot\sqrt{3}\cdot\left(\cos(\varphi_A)\cdot r_m + \sin(\varphi_A)\cdot(L_y - r_m)\right)} \tag{23}$$

4.4 Validation of theoretical models

To validate the theoretical models, ME1C, ME2C, and MA2P, a finite element model of a strip of a lipped channel section was developed. This model used the same overall set-up as the finite element models described in Section 3. The model geometry and the specific boundary conditions are shown in figure 16.

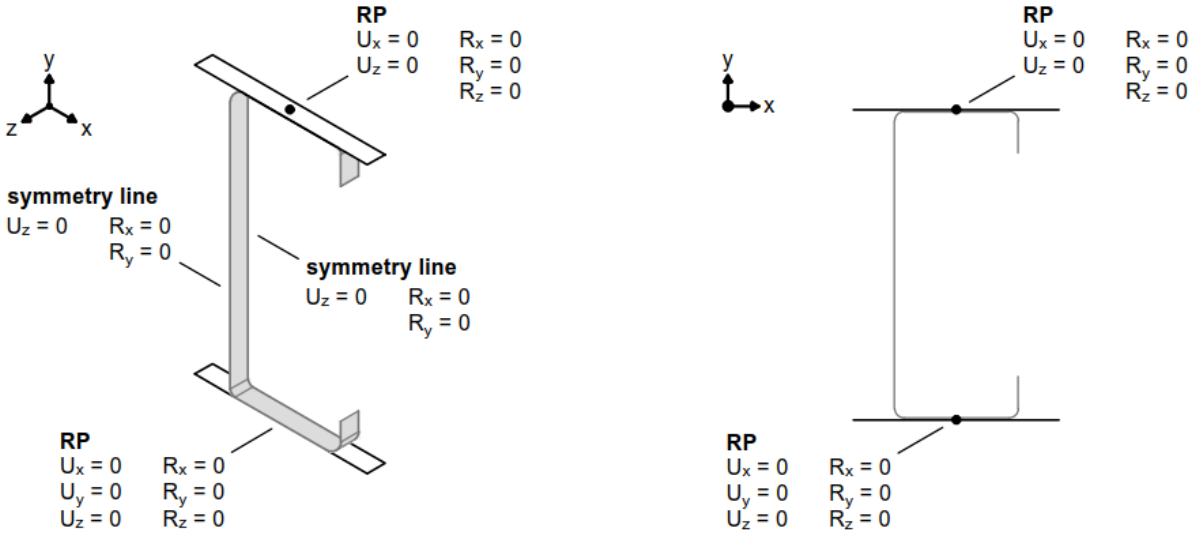

Figure 16. Boundary conditions for the strip model. RP stands for Reference Point, Abaqus specific (Dassault Systems, 2017): (a) isometric view; (b) cross-sectional view.

For the experiments conducted by Sundararajah (2017), the average geometric and mechanical properties are presented in Table 1. Based on these properties, the load-web crippling behaviour of a strip of the lipped channel section was obtained from both the theoretical and finite element models. In the finite element simulations, the yield line occurred at half the section height (thus note that for all cases the yield-arc deformation mode occurred), and consequently the same position was used in the theoretical models.

For validation, the theoretical plastic mechanism initiation load, defined as the intersection between the elastic and plastic load-web crippling deformation curves (figure 17(a)), was compared with the ultimate load from the finite element simulations. When using first-order elasticity (M1EC-MA2P) figure 17(c) shows that correlation is good but a non-unity correction factor or slope *m,* as given by equations (24) and (25) is needed. Second-order elasticity performs well as shown in figure 17(b). This validates the theoretical models and shows that stability related second-order elastic effects play an essential role in predicting the mechanism initiation load correctly with respect to the absolute values; correlation is good either if first-order or second-order elasticity is used.

$$m = \frac{\sum F_{u,MA2P-MiEC}^{\ 2}}{\sum F_{u,MA2P-MiEC} \cdot F_{u,sim}} \tag{24}$$

$$F_{u,sim} = \frac{F_{u,MA2P-MiEC}}{m} \tag{25}$$

4.5 2D to 3D transformation

The previously discussed theoretical models describe the 2D load-web crippling deformation behaviour of a strip of a lipped channel section with length *dz*. To extend this 2D behaviour to full 3D behaviour along the length, assumptions have to be made on how 2D yield line positions and web-crippling deformation are distributed along the length. For the yield line positions, yield line patterns are modelled as given in figures 12(b) and 13(b), further specified by equations (3) to (6). The web-crippling deformation in EOF load cases is assumed constant over the bottom load bearing plate width. Then it is assumed to linearly decrease along the specimen length to become zero at either for elastic behaviour: the reinforced web (figure 18(a)), or for plasticity: at the yield line end L_A (figure

18(b)). For IOF loading, the same principles are followed, except that web crippling deformation will be zero along the end load bearing plate width and will increase to the full web crippling deformation at the interior load bearing plate.

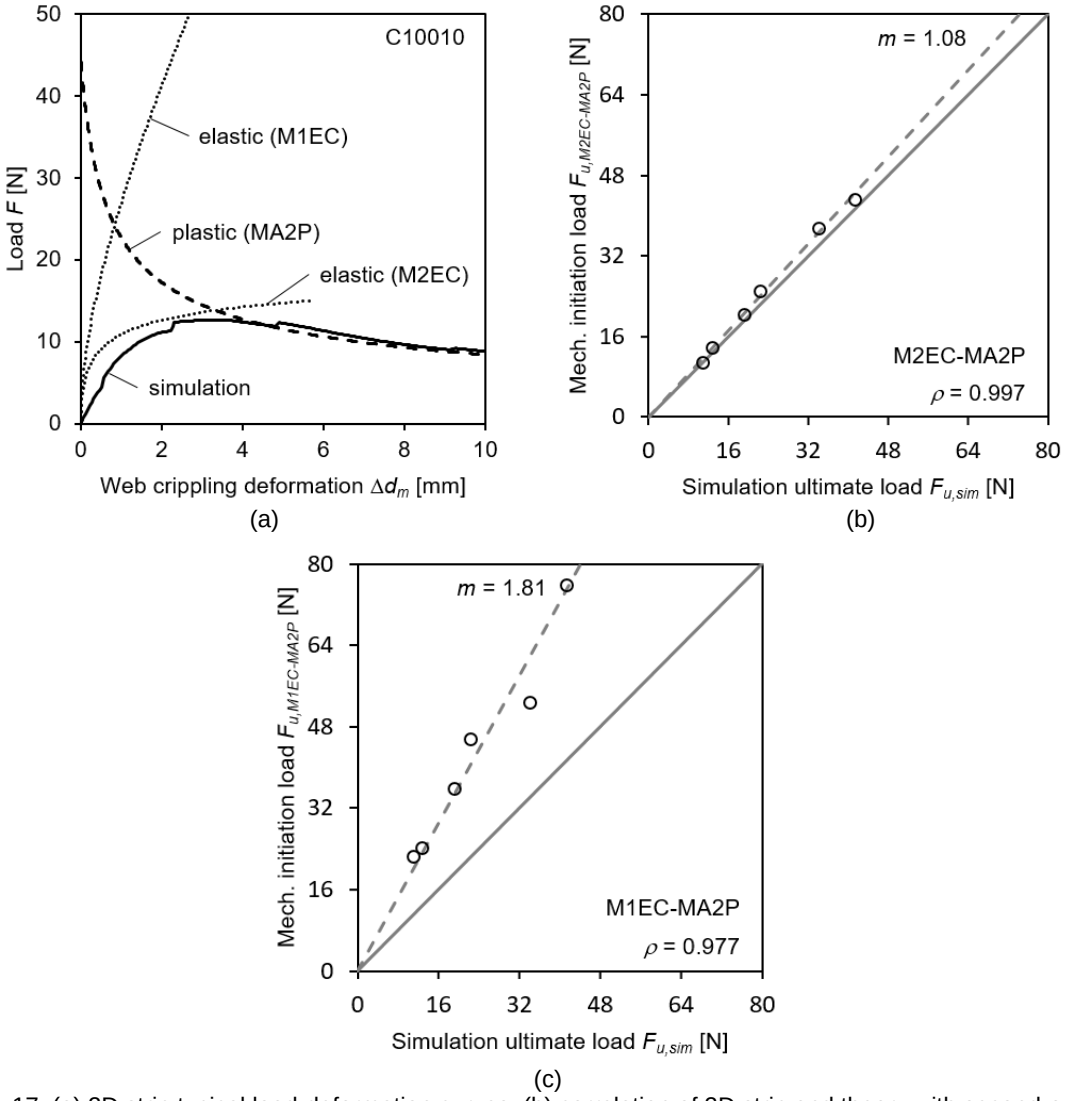

Figure 17. (a) 2D strip typical load-deformation curves; (b) correlation of 2D strip and theory with second-order elasticity; (c) similar with only first-order elasticity.

The 3D model has been implemented as follows. For the EOF load case, elastic curves were determined by the 2D model separately for the part above the load bearing plate, and for the part adjacent to the loading bearing plate. Then both curves were combined —weighted to different degrees of average web crippling deformation as shown in figure 18, i.e. the above load bearing plate part with factor 1, the adjacent part with average factor 1/2— together forming the composed elastic curve. The composed plastic curve was determined using the same approach, using for both parts the yield line distance as shown in figure 12(b). The intersection of the composed elastic and plastic curves has then been used for the prediction of the mechanism initiation load. For the IOF load case, a similar approach was used, however the two plastic curves here, one for each part, use a different yield line position as shown in figure 13(b): the loading plate part uses L_y-r_m, whereas the adjacent part applies the average 1/2 (L_y-r_m). Note that all elastic and plastic curves are non-linear and thus the above applied superposition is a simplification. However, real numerical integration along the length of the behaviour of strips would mean that (due to finding a strength and a corresponding web crippling deformation for each strip) the web crippling deformation distribution along the length would possibly not correspond with the observed and assumed distribution.

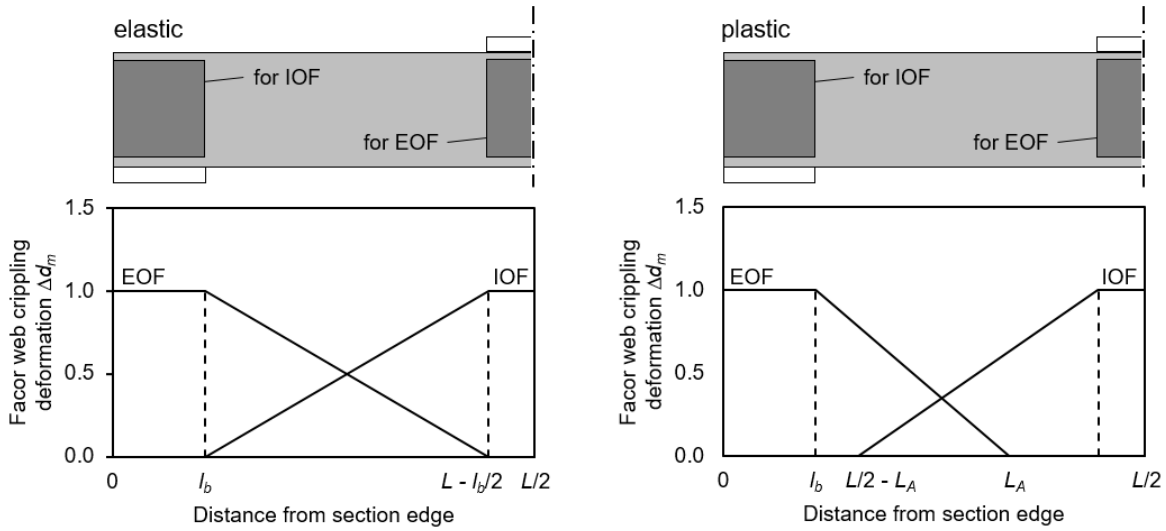

Figure 18. Modelled web crippling deformation along the section length for (a) elastic; and (b) plastic behaviour.

Results of the above approach are given in figure 19. Using first-order elasticity, for EOF always an intersection between elastic and plastic curve could be found, whereas for IOF for all experiments with a load bearing plate of 25 mm (thus showing the rolling mode) and for a few others no intersection could be found. Using second-order elasticity, also for EOF experiments with a load bearing plate width of 25 mm no intersection could be found, and for IOF hardly any experiment gave a result (Heurkens, 2017). The results that are available, though, provide a very well correlated prediction without any corrections as shown in figure 19: The mechanism initiation loads $F_{y;tep1}$ (using first-order elasticity) and $F_{y;tep2}$ (using second-order elasticity) correlate well with ρ = 0.947 and 0.986 to the simulation ultimate loads respectively. For the IOF load case, first-order elasticity performs well with ρ = 0.978 too. However, it should be noted that the rolling mode is excluded from these conclusions, for the reasons given above. It will be shown in section 5 that the rolling mode still can be predicted by a so-called rigid plastic load (which is also the most suitable candidate for DSM applications).

It is noted that for 2D strip behaviour, second-order elasticity performs clearly better than first-order elasticity, whereas for 3D behaviour the situation is reversed, at least for the EOF load case. Likely, instability plays an even larger role for a cross-sectional strip (as this is almost a column) than for a full 3D section, and secondly, the above-mentioned superposition may cause errors in the 3D model. Nevertheless, as will be explained in the next section, a second-order elastic approach is not deemed appropriate for DSM applications, and the first-order approach, shown to have a high correlation here, can be used with confidence, among other approaches.

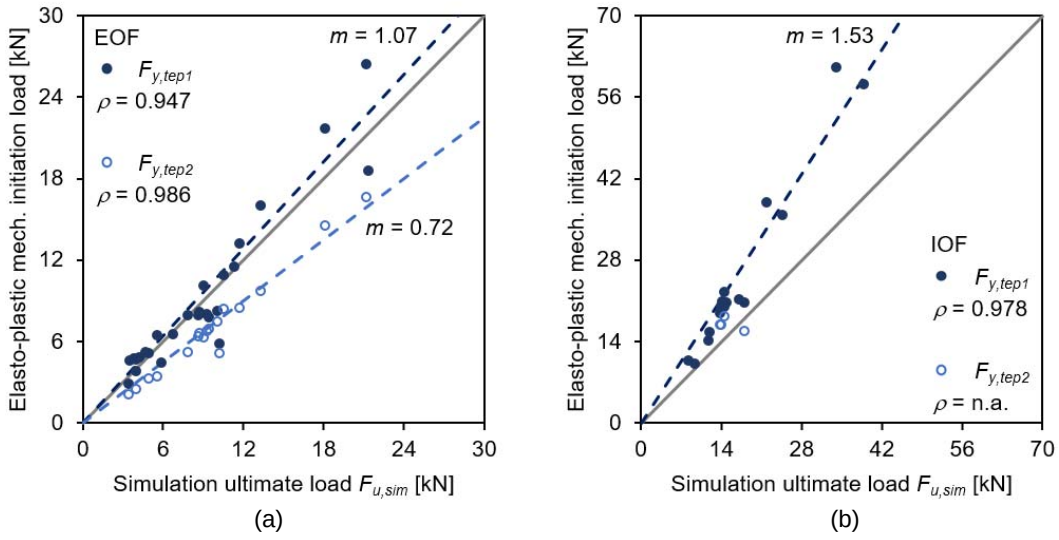

Figure 19. Mechanism initiation loads by model M1EC-MA2P ($F_{y,tep1}$) and M2EC-MA2P ($F_{y,tep2}$) versus simulations for (a) EOF; and (b) IOF load cases.

5 Direct strength method (DSM)

5.1 Calibration data

As mentioned earlier, the DSM requires a buckling load F_{cr} (representing instability) and, at least for members in axial compression or bending, a yield load F_y (which represents strength). Also for web crippling, instability can be indicated by the buckling load, e.g. obtained from finite element analyses as shown in section 3. However, several loads can be chosen for web crippling strength as discussed next:

A first yield load $F_{y,sim}$ obtained from the geometrically non-linear finite element simulations of section 3 can be used. This load is defined as the load at which the first plastic dissipation occurs in the web crippling region. Hence first yield that occasionally occurs just below or above the reinforced webs is neglected. Theoretically, a unit load could be used in a linear finite element simulation. Then the maximum occurring von Mises stress could be scaled up to the yield stress, and the equally scaled unit load is then the first yield load. Heurkens (2017) has shown that both methods give comparable results and here the first method will be used.

A rigid-plastic mechanism initiation load, also named a rigid-plastic load ($F_{y,trp}$), can be used. It neglects elastic behaviour and predicts the onset of a plastic failure mechanism. This load can be predicted by *equilibrium* as stated in model MA2P and assuming zero web crippling deformation Δd_m = 0. A similar approach was employed by Natário et al. (2015) for web crippling, who alternatively used *the principle of virtual work* to find the equilibrium path. Note that this load can be found with the theoretical models for all experiments, as no intersection needs to be found between elastic and plastic curves, see section 4.5.

A first-order elasto-plastic mechanism initiation load ($F_{y,tep1}$) or a second-order elasto-plastic mechanism initiation load ($F_{y,tep2}$) as presented in section 4 can be used. Note that different from all other loads so far, a second-order elasto-plastic mechanism load represents not only strength, but also certain aspects of instability. Hence its application in the DSM may not be a consistent approach. Furthermore, it is possible that for some experiments these loads cannot be found with the theoretical models, as sometimes no intersection can be found between elastic and plastic curves, see section 4.5.

Although often the case, mechanism initiation loads need not be similar to the ultimate load. For instance, the plastic curve of the rolling post-failure mode may increase significantly after mechanism initiation, only thereafter to decrease again, see figure 7(b). Since no theoretical models exist to predict such ultimate loads as a maximum in a plastic curve, ultimate loads are not considered here.

5.2 DSM calibration

Several DSM equations have been calibrated using the results from the finite element simulations of the lipped channel sections subject to EOF and IOF load cases: Equations (26) to (29) originate from AISI S100 (2016); equation (30) comes from Duarte and Silvestre (2013), and equation (31) was used by Natário *et al.* (2015). All equations are valid for $\lambda \geq \lambda_0$, with $\lambda = \sqrt{F_y / F_{cr}}$. Note that calibrations could have also been carried out using the experimental results of section 2, but the data set from the finite element simulations is larger and is believed to be more consistent and accurate due to the nature of finite element simulations versus the nature of experimental work.

$$F_n = \left(k_1^{F_y/F_{cr}}\right) \cdot F_y \quad (26)$$

$$F_n = k_1 \cdot F_{cr} \quad (27)$$

$$F_n = \left(1 - k_1 \cdot \left(\frac{F_{cr}}{F_y}\right)^{k_2}\right) \cdot \left(\frac{F_{cr}}{F_y}\right)^{k_2} \cdot F_y \quad (28)$$

$$F_n = k_1 \cdot F_y \cdot \left(1 - k_2 \cdot \frac{F_y}{F_{cr}}\right) \quad (29)$$

$$F_n = \left(\frac{k_1}{\sqrt{F_y / F_{cr}}} - \frac{k_2 \cdot F_{cr}}{F_y}\right) \cdot F_y \quad (30)$$

$$F_n = k_1 \cdot \left(1 - k_2 \cdot \left(\frac{F_{cr}}{F_y}\right)^{k_3}\right) \cdot \left(\frac{F_{cr}}{F_y}\right)^{k_3} \cdot F_y \quad (31)$$

Calibration of the DSM equations practically means finding values for the k_i-factors. This has been conducted with SPSS statistical software, based on a least squares approach. Goodness of fit has

been assessed by reviewing the residual plot, in combination with the coefficient of determination R^2. equation (31) fits the calibration data best, independent of the yield load definition ($F_{y,sim}$, $F_{y,trp}$, $F_{y,tep1}$, or $F_{y,tep2}$), and its results are shown in figures 20 and 21 for EOF and IOF load cases. Results using $F_{y,tep2}$ are not displayed as the data points did span only a very narrow slenderness range for EOF load cases and in many cases, as explained in section 4.5, no mechanism initiation load was found for IOF load cases. Some DSM curves needed a slenderness restriction λ_0 at the curve maximum, as otherwise decreasing normalized strength values were found for further decreasing slenderness.

As explained in the introduction, a clear trend exists between the ultimate load of a member and its slenderness in the application of DSM for axial compression and bending. For web crippling, it depends on the type of yield load used (figures 20 and 21). When using the first yield load ($F_{y,sim}$), the slenderness remains about constant, while the normalized strength varies. This results in a vertical cluster of data points, as shown in figure 20(a) and 21(a). Using the rigid plastic load ($F_{y,trp}$) as yield load, the slenderness varies between 0.5 and 1.8 and the normalised strength varies between 0.5 to 1.0, and a clear trend becomes visible, figure 20(b) and 21(b). The first order elasto-plastic load ($F_{y,tep1}$) results in the data points clustered more closely together, as shown in figure 20(c) and 21(c). In conclusion, the rigid plastic load most closely matches the trend on which the DSM is based.

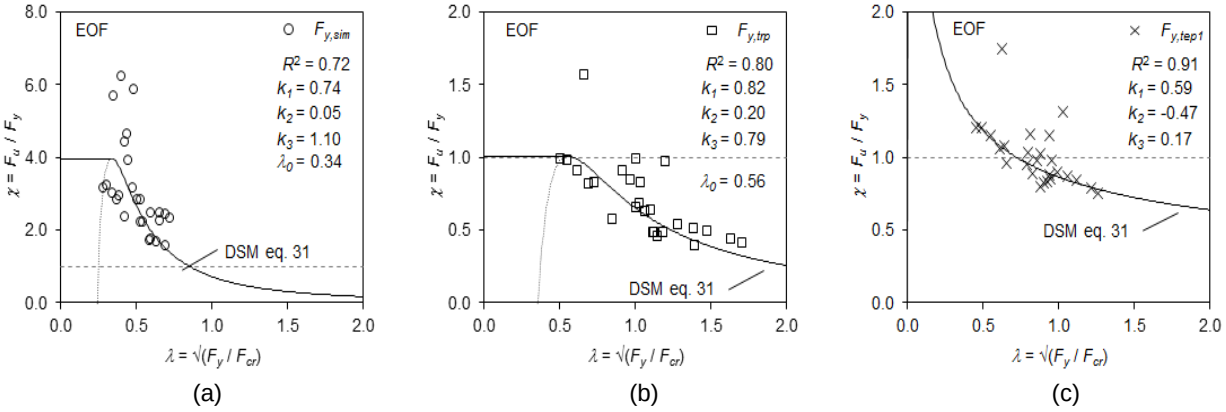

Figure 20. DSM curves for the EOF load case based on equation (31) using: (a) first yield load; (b) rigid plastic load; (c) first order elasto-plastic load.

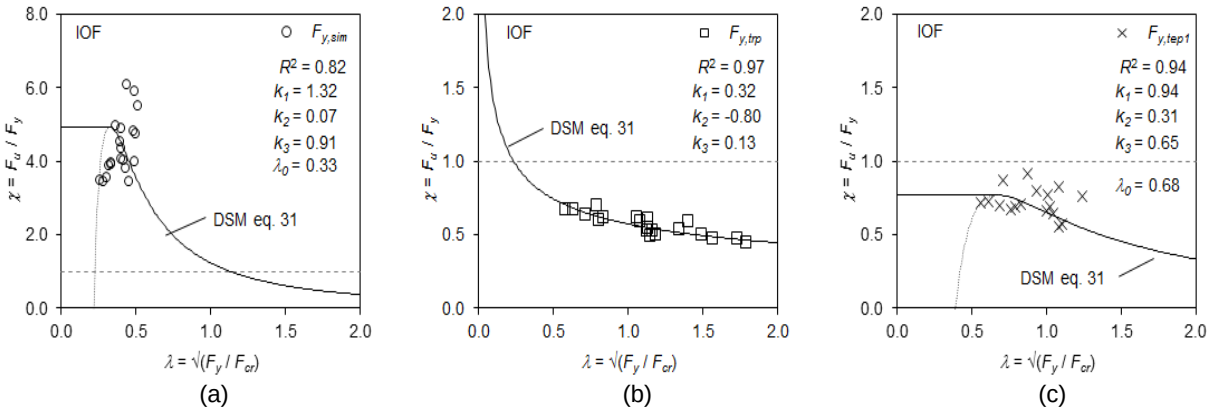

Figure 21. DSM curves for the IOF load case based on equation (31) using: (a) first yield load; (b) rigid plastic load; (c) first order elasto-plastic load.: (a)

5.3 Comparison

Table 5 and figure 22 present methods to predict the web crippling strengths under EOF and IOF load cases. The theoretical 2D elasto-plastic models that are integrated along the section length ($F_{y,tep1}$ and $F_{y,tep2}$) correlate very well with the simulations (and thus experiments), regardless of whether first-order or second-order elasticity is taken into account. However, the mean, to be corrected by a correction factor m, is not so good for first-order elasticity and the IOF load case, and second-order elasticity and the EOF load case. For DSM ultimate load predictions, the correlation depends clearly on the type of yield load used. Using first yield ($F_{u,sim,dsm}$) seems to be least useful. For the EOF load case, a first-

order elasto-plastic mechanism initiation load ($F_{u,tep1,dsm}$) performs best, while the rigid plastic mechanism initiation load ($F_{u,trp,dsm}$) performs best for the IOF load case. As explained, a second-order mechanism initiation load could not be used due to practical considerations. This is not such a large issue since applying it for the yield load in the DSM (which also uses the buckling load) is not a consistent approach (instability is taken into account twice). Classic (i.e. using curve-fitting rules, not DSM) Eurocode 3 and AISI S100 predictions ($F_{u,EC3}$ and $F_{u,S100}$) correlate well but are quite conservative and unconservative, respectively. Finally, predictions following a classic Merchant-Rankine approach ($F_{u,m-r}$), based on equation 32, and using the rigid plastic mechanism initiation load for F_y, are quite conservative.

$$F_{u,m-r} = \frac{F_y}{1+F_y/F_{cr}} \tag{32}$$

Table 5. Numerical comparison of predicted and simulation ultimate loads.

Yield load	EOF correl. ρ $F_{u,sim}$	mean μ $F_{y,i}$ / $F_{u,sim}$	st.dev. σ $F_{y,i}$ / $F_{u,sim}$	IOF correl. ρ $F_{u,sim}$	mean μ $F_{y,i}$ / $F_{u,sim}$	st.dev. σ $F_{y,i}$ / $F_{u,sim}$
$F_{y,tep1}$	0.947	1.02	0.18	0.978	1.40	0.19
$F_{y,tep2}$	0.986	0.71	0.08	n.a.	1.14	0.18
$F_{u,sim,dsm}$	0.870	0.92	0.26	0.919	0.94	0.22
$F_{u,trp,dsm}$	0.910	0.94	0.20	0.988	0.97	0.07
$F_{u,tep1,dsm}$	0.959	0.96	0.13	0.980	0.95	0.13
$F_{u,EC3}$	0.981	0.60	0.08	0.974	0.79	0.11
$F_{u,S100}$	0.943	1.18	0.20	0.964	1.05	0.14
$F_{u,m-r}$	0.909	0.73	0.15	0.959	0.78	0.17

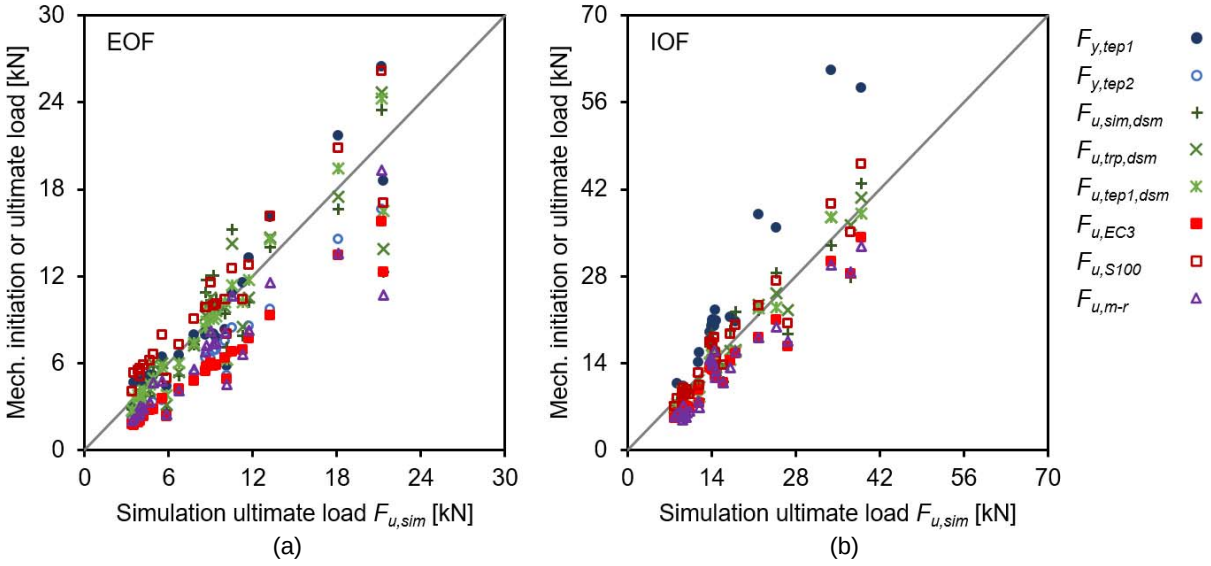

Figure 22. Graphical comparison of predicted and simulation ultimate loads: (a) EOF and (b) IOF.

5.4 Rolling deformation mode

For most experiments and the extended data set (the latter using only l_{lb}=50 mm), the yield-arc deformation mode occurred, and for this deformation mode the conclusions in this section 5 so far are valid. However, the rolling deformation mode, only occurring for IOF for l_{lb} = 25 mm, should be discussed as well: In section 3.4 it was mentioned that for the rolling mode, yield line distances and prolongations could not be measured, and thus the formulae for deriving these quantities were based on experiments showing the yield-arc deformation mode only. Secondly, section 4.3 explained that it was assumed that the yield-arc second order plastic model could also be used for the rolling mode. Finally, in this section this yield-arc plastic model, using the distance and prolongation formulae inevitably based on the yield-arc mode too, was used for the DSM-equations, and thus was applied to both the yield-arc and rolling deformation modes.

However, as was explained in 4.5, the theoretical models could not find the first-order and second-order elasto-plastic mechanism initiation loads for the rolling mode. In other words, for comparisons of the DSM-equations with the simulations, experiments with rolling modes were not taken into account, at least not when first- and second-order elasto-plastic mechanism initiation loads were used. Where the rigid-plastic mechanism initiation load ($F_{y,trp}$) was used, also for the rolling mode this load could be found, see table 6. In this table, it can be seen that the yield-arc plastic model, using the distance and prolongation formulae inevitably based on the yield-arc mode, correlates very well with the simulation data for rolling, only a large offset exists between the averages. This is because for the rolling mode, the mechanism initiation load (as predicted by the theory) is often quite smaller than the ultimate load (as given by the simulation). Surprisingly enough, the coefficients in the DSM used for fitting the theory to the simulations for all experiments (yield-arc and rolling), seem to correct this rolling mode specific issue. Namely, when the mechanism initiation load ($F_{y,trp}$) is used as part of the DSM, both correlation and average values are predicted very well, see the last row of table 6.

Table 6. Specific results for the rolling deformation mode.

Section (all under IOF)	l_{lb} [mm]	$F_{u;sim}$ [N]	$F_{y,trp}$ [N]	$F_{u,trp,dsm}$ [N]
C10010	25	7.82	12.79	6.89
C10015	25	14.79	21.69	13.21
C15012	25	10.34	19.27	9.67
C15015	25	15.96	25.35	13.75
C20019	25	26.64	41.95	22.56
C20024	25	37.12	66.64	36.18
Average		18.78	31.28	17.04
Correlation with $F_{u;sim}$			0.99	0.99

l_{lb} = load bearing plate width [mm], $F_{u;sim}$ = simulation ultimate load [N], $F_{y,trp}$ = theoretical rigid-plastic mechanism initiation load [N], $F_{u,trp,dsm}$ = DSM (eq. 31) using $F_{y,trp}$ for web crippling strength [N]

6 Conclusions

A recent experimental study investigated the web crippling behaviour of lipped channel sections made of six different cross-sections under EOF and IOF load cases with three load bearing plate widths (Sundararajah, 2017). Finite element models of the tested lipped channel sections were first developed in this study to predict their buckling load and the elasto-plastic behaviour, and to develop an extended data set of web crippling ultimate strengths. Possible asymmetric behaviour was accounted for and corner radii were modelled accurately by several elements along the radius. An excellent correlation was found between the finite element simulations and the experiments with respect to the ultimate loads, the deformation modes and load-deformation curves.

Theoretical first- and second-order elasto-plastic models were then developed to predict the plastic mechanism initiation of a 2D strip of lipped channel sections. Agreement of these models with finite element simulations of similar 2D strips was excellent. Subsequently, these 2D models were transformed to 3D models by following the modelled yield line patterns and positions observed in the finite element simulations. Both the first- and second-order 3D models correlated very well with the full section simulations, with the second-order model also predicting the absolute values correctly. For the IOF load case, the second-order elastic and plastic load-web crippling curves often did not intersect and thus did not provide a mechanism initiation load.

Several DSM equations as proposed in literature were then calibrated using the results from the finite element simulations with several types used for the yield load as needed in the DSM: A first yield load found via the finite element simulations; a rigid-plastic mechanism initiation load as used by other researchers, and a first-order elasto-plastic mechanism initiation load via the theoretical models developed in this study. The use of the second-order elasto-plastic mechanism initiation load led to practical problems, and besides it was regarded as an inconsistent approach for DSM since instability would have been taken into account twice.

The trend between slenderness and strength, on which the DSM is based, was most clearly found if the rigid-plastic mechanism initiation load was used for the yield load. Since it performs well with respect to correlation and mean values (also for the rolling deformation mode), is closest to a strength only criterion and is successfully used by other researchers also (Natário, 2015; Natário *et al.* 2015), it

seems to be the best candidate for DSM applications. Thus the following final equations are suggested:

$$F_n = 0.82 \cdot \left(1 - 0.20 \cdot \left(\frac{F_{cr}}{F_y}\right)^{0.79}\right) \cdot \left(\frac{F_{cr}}{F_y}\right)^{0.79} \cdot F_y \quad \left(\chi = 1 \text{ if } \lambda < 0.56\right) \quad \text{for EOF} \tag{33}$$

$$F_n = 0.32 \cdot \left(1 + 0.80 \cdot \left(\frac{F_{cr}}{F_y}\right)^{0.13}\right) \cdot \left(\frac{F_{cr}}{F_y}\right)^{0.13} \cdot F_y \quad \text{for IOF} \tag{34}$$

with F_y being the rigid-plastic mechanism initiation load as calculated in section 4.

The calibrated DSM approach (with all its alternatives for the yield load) was compared with the theoretical models and design codes. Even under academic conditions (e.g. simulations instead of experiments, first yield exactly determined, etc.) the DSM does not perform better than relatively simple theoretical models for the EOF load case, but performs better than the current design equations, the Merchant-Rankine approach and the IOF theoretical models. The DSM approach has been shown to perform very well for members under compression and bending, and is intuitively and relatively easy to use. Hence arguments may be valid to try and widen its scope, thus including web-crippling of lipped channel sections under EOF and IOF loading. This paper has shown that this is possible with more than acceptable correlations. The theoretical models also provide a strong argument for the DSM. A second-order model was needed to find both high correlation and a near unity correction factor, thus instability plays a significant role in web crippling. If this second-order model is thought to be too complex, the next alternative that takes into account instability is the DSM.

7 Recommendations and future work

More experiments or simulations on lipped channel sections should be conducted, thus spanning a wide geometrical and material property range. This will provide additional insight in the yield line patterns and load-web crippling deformation behaviour. DSM calibrations and applicability will also be improved.

The theoretical models as used in this research could be improved, especially with regards to the 2D to 3D transformations. This paper has assumed a relatively basic yield line pattern. Load-web crippling deformation may also be described more accurately with plate theory.

Finally, it should be investigated further why and under which conditions (a) the theoretical yield-arc model performs so well for rolling too; and (b) coefficients in the DSM, used for fitting the theory to the simulations of all experiments (yield-arc and rolling), correct the rolling specific issue that the mechanism initiation load is much lower than the ultimate load.

Acknowledgements

The authors wish to thank Mr. L. Sundararajah for providing his experimental data for use in this study.

References

AISI S100 (2016): AISI S100-16: North American Specification for the Design of Cold-Formed Steel Structural Members. Washington, USA: American Iron and Steel Institute (AISI).

AISI S909 (2013): AISI S909-13 – Standard Test Method for Determining the Web Crippling Strength of Cold-Formed Steel Beams. Washington, USA: American Iron and Steel Institute (AISI).

Anil Kumar, M.V., Kalyanaraman, V. (2010). Evaluation of Direct Strength Method for CFS Compression Members without Stiffeners, Journal of Structural Engineering, 136(7), 879–885.

Bakker, M.C.M. & Stark, J.W.B. (1994). Theoretical and Experimental Research on Web Crippling of Cold-Formed Flexural Steel Members. Thin-Walled Structures, 18, 261-290.

Becque, J., Lecce, M., Rasmussen, K.J.R. (2008). The direct strength method for stainless steel compression members. Journal of Constructional Steel Research, 64(11), 1231-1238.

CEN European Committee for Standardization (2006). EN 1993-1-3:2006, Eurocode 3: Design of steel structures - Part 1-3: General rules - Supplementary rules for cold-formed members and sheeting, CEN, Brussels, Belgium.

Dassault Systems (2017). Abaqus/Standard and Abaqus/CAE, https://www.3ds.com/products-services/simulia/products/abaqus.

Duarte, A.P.C., & Silvestre, N. (2013). A New Slenderness-Based Approach for the Web Crippling Design of Plain Channel Steel Beams. International Journal of Steel Structures, 13, 421-434.

Gunalan, S., & Mahendran, M. (2015). Web Crippling Tests of Cold-Formed Steel Channels Under Two Flange Load Cases. Journal of Constructional Steel Research, 110, 1-15.

Hancock, G.J., Kwon, Y.B., & Bernard, E.S. (1994). Strength Design Curves for Thin-Walled Sections Undergoing Distortional Buckling. Journal of Constructional Steel Research, 31, 169-186.

Heurkens, R.A.J. (2017). Direct Strength Method for Lipped Channel Sections under EOF and IOF Web Crippling Loading. M.Sc.-thesis Eindhoven University of Technology, Department of the Built Environment, Unit Structural Design, Eindhoven, The Netherlands.

Hofmeyer, H. (2005). Cross-Section Crushing Behaviour of Hat-Sections (Part II: Analytical Modelling). Thin-Walled Structures, 43, 1155-1165.

Hofmeyer, H., Kerstens, J.G.M., Snijder, H.H., & Bakker, M.C.M. (2002). Combined Web Crippling and Bending Moment Failure of First-Generation Trapezoidal Steel Sheeting. Journal of Constructional Steel Research, 58, 1509-1529.

Joint Technical Committee BD-082, Cold-formed Steel Structures (2005). AS/NZS 4600:2005 Australian/New Zealand Standard Cold-formed steel structures, Standards Australia, Sydney, and Standards New Zealand, Wellington.

Keerthan, P., Mahendran, M. & Steau, E. (2014) Experimental studies on web crippling behaviour of hollow flange channel beams under two flange load cases. *Thin-Walled Structures*, *85*, pp. 207-219.

Keerthan, P., Mahendran, M., & Steau, E. (2014). Experimental Study of Web Crippling Behaviour of Hollow Flange Channel Beams Under Two Flange Load Cases. Thin-Walled Structures, 85, 207-219.

Kwon, Y.B., Kim, B.S., Hancock, G.J. (2009). Compression tests of high strength cold-formed steel channels with buckling interaction. Journal of Constructional Steel Research, 65(2), 278-289.

Moen, C.D., Schafer, B.W. (2009). Elastic buckling of thin plates with holes in compression or bending, In Thin-Walled Structures, 47(12), 1597-1607.

Natário, P. (2015). Localized Failure of Thin-Walled Steel Members Subjected to Concentrated Loads: Analysis, behaviour and Design. Ph.D. thesis University of Lisbon, Portugal.

Natário, P., Silvestre, N., & Camotim, D. (2015). Direct Strength Prediction of Web Crippling Failure of Beams Under ETF Loading. Thin-Walled Structures, 98, 360-374.

Prabakaran, K., & Schuster, R. (1998). Web Crippling of Cold-Formed Steel Members. Proceedings Fourteenth International Specialty Conference on Cold-Formed Steel Structures, October 15-16, 1998, St. Louis, USA.

Ranawaka, T., Mahendran, M. (2009). Distortional buckling tests of cold-formed steel compression members at elevated temperatures. Journal of Constructional Steel Research, 65(2), 249-259.

Rusch, A., & Lindner, J. (2001). Remarks to the Direct Strength Method. Thin-Walled Structures, 39, 807-820.

Schafer, B.W. & Peköz, T. (1998). Direct Strength Prediction of Cold-Formed Steel Members Using Numerical Elastic Buckling Solutions. Proceedings 14th International Specialty Conference on Cold-Formed Steel Structures, October 15-16, St. Louis, MO, USA.

Schafer, B.W. (2008). Review: The Direct Strength Method of Cold-Formed Steel Member Design. Journal of Constructional Steel Research, 64, 766-778.

Shahbazian, A., Wang, Y.C. (2011). Application of the Direct Strength Method to local buckling resistance of thin-walled steel members with non-uniform elevated temperatures under axial compression. Thin-Walled Structures, 49(12), 1573-1583.

Sundararajah, L. (2017). Web Crippling Studies of Cold-Formed Steel Channel Beams - Experiments, Numerical Analyses and Design Rules. Ph.D. thesis Queensland University of Technology, Brisbane, Australia.

Sundararajah, L., Mahendran, M., & Keerthan, P. (2015). Experimental Studies of Lipped Channel Beams Subject to Web Crippling Under ETF and ITF Load Cases. Proceedings Eighth International Conference on Advances in Steel Structures, July 21-24, 2015, Lisbon, Portugal.

Sundararajah, L., Mahendran, M., & Keerthan, P. (2017). Web Crippling Experiments of High Strength Lipped Channel Beams under One-Flange Loading, Accepted in Journal of Constructional Steel Research.

Timoshenko, S.P., & Gere, J.M. (1985). Theory of Elastic Stability. New York: McGraw-Hill.

Von Kármán, T., Sechler, E.E., & Donnell, L.H. (1932). The Strength of Thin Plates in Compression. Transactions of the American Society of Mechanical Engineers, 54, APM 54-5, 53-57.

Winter, G. (1947). Strength of Thin Steel Compression Flanges (with Appendix), bulletin 35/3, Cornell University Engineering Experiment Station, Ithaca, NY, USA.

Yang, D., Hancock, G.J. (2004). Compression Tests of High Strength Steel Channel Columns with Interaction between Local and Distortional Buckling, Journal of Structural Engineering**,** 130(12), 1954-1963.

Yap, D.C.Y., Hancock, G.J. (2011). Experimental study of high-strength cold-formed stiffened-web C-sections in compression, Journal of Structural Engineering, 137(2), 162-172.

Young, B., & Hancock, G.J. (1998). Web Crippling Behaviour of Cold-Formed Unlipped Channels. Proceedings 14th International Specialty Conference on Cold-Formed Steel Structures, October 15-16, St. Louis, MO, USA.

Young, B., & Hancock, G.J. (2001). Design of Cold-Formed Channels Subjected to Web Crippling. Journal of Structural Engineering, 127, 1137-1144.

Zhou, F., & Young, B. (2006). Yield Line Mechanism Analysis on Web-Crippling of Cold-Formed Stainless Steel Tubular Sections Under Two-Flange Loading. Engineering Structures, 28, 880-892.